Numerical discretization and assessment of bed load discharge closure equations for transient flow over erodible bed in 1D and 2D situations

Carmelo Juez Jiménez

Máster en Mecánica Aplicada

Programa Oficial de Posgrado en Ingenería Mecánica y de Materiales

Zaragoza, Junio 2012

Director: Dr. Javier Murillo Castarlenas

Curso 2011-2012

Escuela de Ingeniería y Arquitectura Universidad de Zaragoza

Numerical discretization and assessment of bed load discharge closure equations for transient flow over erodible bed in 1D and 2D situations

Abstract

Free surface water flows over rigid bed are traditionally modeled using mass and momentum conservation laws. In the case of deformable bed, the physics of the problem needs to be described in order to define suitable mathematical models. A theoretical framework is developed in the first part of this work, useful to clarify the hypothesis included in the mathematical model used to predict morphodynamic changes. As a consequence, another equation is included to consider the variations in time and space of the bed level. This extra equation is defined using the bed material mass conservation law, where mass fluxes are governed by the dynamics of the surface flow.

When numerically modeling free surface flows with load transport over erodible bed in realistic situations, conventional methods solve the decoupled hydrodynamic and the morphodynamic systems, using splitting techniques. Considering that momentum conservation equations include source terms arising from the variation of the bed level, uncoupled solvers are not adequate for rapidly varying flows, leading to unstable solutions even in cases of moderate transient flows. Therefore, it is necessary to define a completely coupled formulation, able to deal with a full range of hydrodynamic and morphodynamic problems.

Usual formulations for morphodynamic mass fluxes are given by empirical sediment transport laws. The different sediment transport capacity formulae, used worldwide to control the erosion and deposition rates that deform the bed in transient cases, are based on equilibrium closure equations obtained from experimental observation in 1D steady cases. Their general applicability to 2D unsteady problems requires a careful analysis to assess whether they are able to predict sediment transport in complex transient flows. This point is of paramount importance and requires a well tested and robust numerical method.

In response to this necessity, this work focuses on the evaluation of the relative numerical performance of a series of well known sediment transport formulae in laboratory test cases with experimental data. The bed load formulae have been implemented in the framework of a previously developed robust and accurate solver. The reliability of the underlying numerical scheme has been useful to select one of the formulae, when correctly implemented, as the one showing the best behavior of the computed solution in comparison with experimental data.

The present work represents an introduction in the field of sediment transport process modeling and the basis for future developments.

Discretización numérica y aplicabilidad de fórmulas de cierre en flujos transitorios sobre lecho erosionable en configuraciones 1D y 2D

Resumen

Los flujos transitorios sobre lecho rígido son normalmente modelados usando un conjunto de ecuaciones que incluyen las de conservación de masa y cantidad de movimiento. Para el caso de lecho deformable, la física del problema necesita ser descrita de forma matemática a través de diferentes modelos. La primera parte de este trabajo se centra en clarificar las distintas hipótesis asumidas por dichos modelos matemáticos. Como consecuencia de este estudio se deriva la inclusión de una variable en la formulación del problema que incluye la variación de fondo.

En la mayoría de los casos a la hora de modelar el flujo de agua sobre fondo erosionable se suele desacoplar la parte hidrodinámica de la parte morfodinámica. Las soluciones obtenidas con los modelos desacoplados han demostrado ser inadequados para la resolución de flujos transitorios con variaciones rápidas de régimen de flujo, puesto que se generan inestabilidades. En consecuencia, es necesario emplear una formulación acoplada capaz de manejar un rango amplio de situaciones hidrodinámicas y morfodinámicas diferentes.

Un sistema completo y acoplado de ecuaciones diferenciales parciales que incluía las ecuaciones de aguas poco profundas y una ecuación de conservación de masa para el sedimento fue desarrollado en un trabajo previo. Partiendo de este trabajo anterior se han implementado diferentes formulaciones de cierre para calcular el transporte de sedimento. Puesto que dichas formulaciones fueran derivadas de ensayos de laboratorio en situaciones 1D y para situaciones en equilibrio, se impone la necesidad de valorar su efectividad en situaciones transitorias para configuaciones 1D y 2D.

Además de realizar la comparativa entre estas correlaciones empíricas se ha propuesto una nueva discretización para una de ellas, obteniéndose de esta manera unos resultados numéricos más precisos en comparación con los datos experimentales.

Las conclusiones extraídas de este trabajo han permitido comprender mejor la dinámica del transporte de sedimento en flujos de agua y serán utilizadas en un futuro próximo para dotar de mayor complejidad al modelo matemático.

Contents

List of Figures

List of Tables

Chapter 1

Introduction

The science of sediment transport deals with the interrelationship between flowing water and sediment particles. At present, morphological evolution is one of the most active topic in the field of hydraulic research. In special, numerical efforts have been devoted to the simulation of dam break flows over mobile bed. Appropriate closure equations are needed to evaluate the rate of sediment transport, as they are determinant for a correct description of the morphodynamic changes. Experimental investigation based on 1D steady sediment transport laboratory tests is the basis to provide sediment transport formulations, and has lead to a large range of capacity formulae.

On the other hand, mathematical models have been developed in last years under different approaches. The improvement of the computer technology has allowed to reformulate the earliest 1D models (Cunge *et al.*, 1980; De Vriend *et al.*, 1993) into more sophisticated ones (Z. Cao, 2002), also making possible 2D computation of the sediment transport in alluvial streams (Begnudelli *et al.*, 2010; Wu & Wang, 2004). An overview of 1D and 2D modeling approaches for river morphodynamics is presented by Wu (2007), where attention is focused on non-equilibrium state formulations where the bed evolution depends on the difference between the actual transported material and the equilibrium sediment transport capacity. Different authors have suggested to include this feature by means of the definition of an adaptation length, which can be formulated through deterministic laws (Wu & Wang, 2004; Armanini & Di Silvio, 1988; Greimann *et al.*, 2008) or by the dominant dimensions of the sediment movement, the bed forms or the channel geometry (Wu, 2007). Numerical results indicate that it is possible to obtain accurate results at the cost of selecting the appropriate adaptation length (Z. Cao, 2002; Wu & Wang, 2004; Xia *et al.*, 2010). Begnudelli *et al.* (2010) pointed out that the applicability of the non-equilibrium formulation depends on the magnitude of the length scales in relation to the scales that must be resolved by the model.

The complexity of non-equilibrium formulations can be avoided assuming that the transported material discharge is at any time given by the capacity formulae obtained from experimental one dimensional steady flows. Moreover it has to be remarked that this sediment transport is approximated as bed load, without considering a separate sediment transport layer which includes the suspension transport.

Several sediment transport capacity formulae are available in the specialized literature (Meyer-Peter & Müller, 1948; Ashida & Michiue, 1972; Camenen & Larson, 2005; Luque & van Beek, 1976; Parker, 1979; Nielsen, 1992; Smart, 1984; Wong, 2003), each one arising from different laboratory and field data sets and developed for a limited range of conditions. This work is focused on analyzing the differences among more commonly used formulae, using a previously defined and tested numerical scheme (Murillo & García-Navarro, 2010), able to handle correctly with all range of hydrodynamic and morphodynamic problems, limiting in this way, the possible interferences between numerical modeling and sediment transport capacity formulation performance. Not only 1D situations are studied, but also 2D cases are numerically explored in order to test the validity of this closure formulae for bidimensional flows.

The outline of the present work is as follows: in chapter 2 different mathematical models are described in order to clarify the assumptions made in these type of flow, leading to as suitable description of the problem by means of a reduced set of partial differential equations. In Chapter 3 the bed load formulations employed in this work are described, and are written using a differentiable expression. Chapter 4 presents the numerical scheme used to solve the mathematical model selected, that includes the shallow water equations and the Exner equation. Chapter 5 displays the numerical results in one dimensional test cases and chapter 6 extends to bidimensional test cases, comparing always with experimental data. Finally, in chapter 7 the conclusions and further research are discussed.

Chapter 2

Mathematical model

2.1 Introduction

In this chapter the mathematical model which governs the dynamics of the sediment transport problem will be described. The equations express the depth averaging of the mass and momentum conservation laws, under the hypothesis of hydrostatic pressure and negligible vertical accelerations (SWE) and are extended to include the morphodynamic evolution of the bed.

Along this chapter, the physics of the problem is analyzed departing from a general and complex two fluid layer model, where the set of equations is reduced ending up in a one fluid layer model coupled with the bed evolution Exner equation. First, for the sake of clarity, the formulation is presented considering only the vertical plane and 1D flow. Then, the extension to 2D situations is indicated.

2.2 Two layer model

The model involves the following assumptions:

i) Based on experimental observations (Fraccarollo & Capart, 2002), and as a first assumption, the flow is considered stratified and composed by two fluid layers (hence the name of the model) and one solid layer, as shown in Figure 2.1. The upper liquid-solid layer is called the suspended layer of thickness h_1: the heterogeneous liquid-granular flow behaves as an effective medium with little slip between water and transport layer, sediment transport is produced by suspension. The medium layer, of thickness h_2, will be referred to as transport layer: the sediment phase is mostly transported as bed load, supported by frictional and collisional grain-grain interactions. The lower layer, defined by the position of the bed level, z, is commonly defined as the morphodynamic layer: the bed boundary is viewed as a transition between two mediums with different behaviors, the solid phase and the fluid phase.

ii) Both upper layers transport granular material, with variable size and density. The amount of granular material transported is defined by means of the depth averaged

volumetric concentration, ϕ.

2.2.1 1D Conservation equations

The domain is divided in three layers, Figure 2.1, limited by interfaces. Interface Γ_w is the air-water/suspended load boundary at the flow free surface. Interface Γ_s defines the upper limit of the transport layer, separating the low concentration layer above from the high concentration liquid-granular mixture below. The third interface, Γ_b, acts as a boundary between the fluid and the solid behavior.

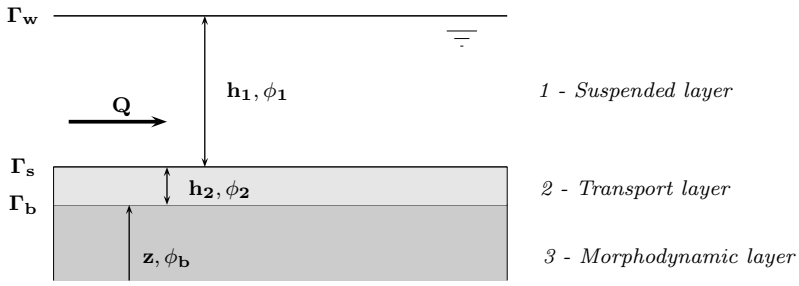

Figure 2.1: Interfaces in the domain

Every layer between the interfaces has its own depth (h_1, h_2, z), depth averaged velocity (u_1, u_2) and depth averaged concentration (ϕ_1, ϕ_2, ϕ_b).

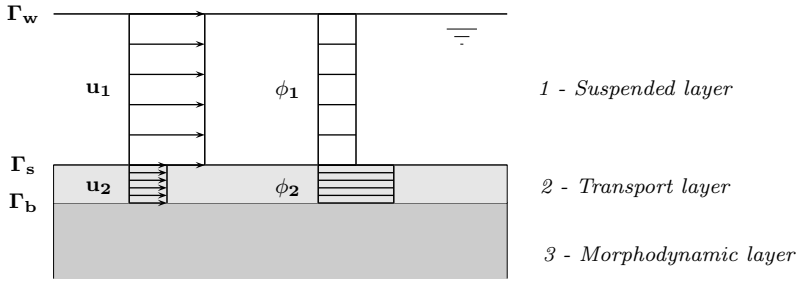

Figure 2.2: Depth averaged quantities within the layers

Through these interfaces solid material exchanges take place.

Mass conservation

The balance of mass applied in an arbitrary control volume, Ω, using the Reynolds transport theorem, yields the general integral equation

$$\frac{\partial}{\partial t}\int_{\Omega}\rho(x,t)d\Omega = 0 \Leftrightarrow \frac{\partial}{\partial t}\int_{\Omega}\rho d\Omega + \int_{\Gamma}\rho u_r n d\Gamma = 0 \tag{2.1}$$

where Γ are the sections across fluxes interact (mobile boundaries and fixed boundaries), ρ is the mass density, u_r is the relative velocity between the flow velocity and the speed of boundary Γ (u_r = u - v) and n is the outward unit vector normal to Γ. For a better comprehension Figure 2.3 is plotted below.

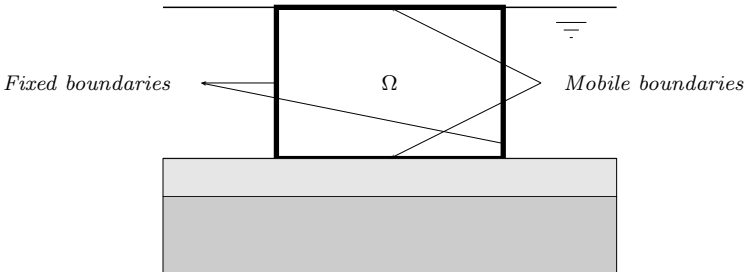

Figure 2.3: Reynolds theorem applied in an arbitrary volume

Applying (2.1) to the spatial control volume of layer 1, the following integral formula is obtained

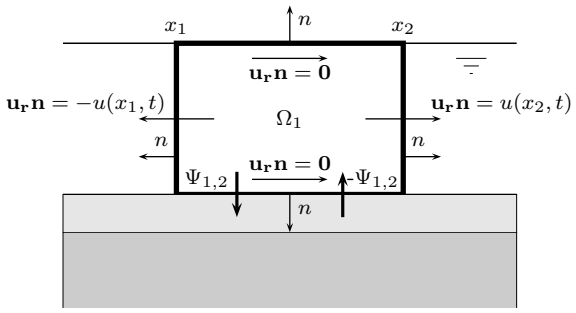

Figure 2.4: Mass conservation in layer 1

$$\underbrace{\frac{d}{dt}\int_{x_1}^{x_2}\int_{A_1(x,t)}\rho_1 dA dx}_{\textit{Local variation}} + \underbrace{\int_{A_1(x_1,t)} -\rho_1 u dS}_{\textit{Flow boundary fixed 1}} + \underbrace{\int_{A_1(x_2,t)}\rho_1 u dS}_{\textit{Flow boundary fixed 2}} + \underbrace{+\int_{x_1}^{x_2}\left\{-(B\rho_1\Psi_{2,1}) + (B\rho_1\Psi_{1,2})\right\}dx}_{\textit{Flow bottom}} = 0 \tag{2.2}$$

where $A_1(x,t)$, $A_2(x,t)$ are the crossed areas, located at coordinates x_1 and x_2, respectively, and B is the width.

The convective inertia term has been split in two contributions, the first one belongs to the fixed boundaries (horizontal flows) and the second one to the mobile boundaries (vertical flows). In the horizontal exchange the relative velocity u_r is equal to u, the

flow velocity, because the speed of boundary is equal to zero, due to is fixed. In the vertical exchange u_r is the difference between the two velocities. The term of u_r is rewritten as a flow per unit length, $\Psi_{i,j} = \frac{Q}{A}$, where Q is the flow, A is the transversal section equal to Bdx, being B the width. Hence, the product $\rho\Psi_{i,j}$ is just a material flux per unit area.

After time integrating, applying Leibnitz rule, the width B is eliminated and the integral form of mass conservation in layer 1 is rewritten as

$$\int_{t_1}^{t_2}\int_{x_1}^{x_2}\frac{\partial}{\partial t}(\rho_1 h_1)dxdt + \int_{t_1}^{t_2}\int_{x_1}^{x_2}\frac{\partial}{\partial x}(\rho_1 h_1 u_1)dxdt - \\ - \int_{t_1}^{t_2}\int_{x_1}^{x_2}\rho_1\Psi_{2,1}^{net}dxdt = 0 \tag{2.3}$$

In differential form is expressed as

$$\frac{\partial(\rho_1 h_1)}{\partial t} + \frac{\partial(\rho_1 h_1 u_1)}{\partial x} - \rho_1\Psi_{2,1}^{net} = 0 \tag{2.4}$$

Splitting the above formulation in its two components, the differential equations are expressed as one part of sediment material (2.5) and another part of water (2.6)

$$\frac{\partial(\rho_1 h_1 \phi_1)}{\partial t} + \frac{\partial(\rho_1 h_1 \phi_1 u_1)}{\partial x} - \rho_1\Psi_{s_{2,1}}^{net} = 0 \tag{2.5}$$

$$\frac{\partial(\rho_1 h_1 (1-\phi_1))}{\partial t} + \frac{\partial(\rho_1 h_1 (1-\phi_1) u_1)}{\partial x} - \rho_1\Psi_{w_{2,1}}^{net} = 0 \tag{2.6}$$

Following the same procedure the mass conservation for layer 2, Figure 2.5, leads to

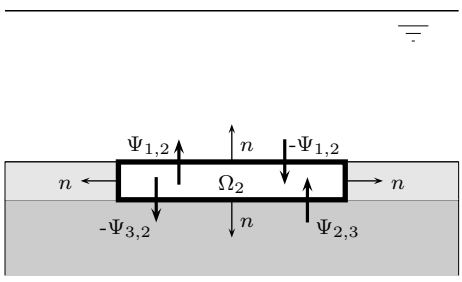

Figure 2.5: Mass conservation in layer 2

$$\frac{\partial(\rho_2 h_2)}{\partial t} + \frac{\partial(\rho_2 h_2 u_2)}{\partial x} - \rho_2\Psi_{3,2}^{net} + \rho_2\Psi_{2,1}^{net} = 0 \tag{2.7}$$

and finally for layer 3

$$\frac{\partial(\rho_b z \phi_b)}{\partial t} + \rho_b \Psi_{3,2}^{net} = 0 \tag{2.8}$$

Momentum conservation

The balance of linear momentum, (2.9), applied in an arbitrary control volume, Ω, using the Reynolds transport theorem, yields the general integral equation

$$\frac{d}{dt}(P) = \frac{d}{dt}\int_{\Omega} \rho u d\Omega \tag{2.9}$$

$$\frac{\partial}{\partial t}\int_{\Omega} \rho u d\Omega + \int_{\Gamma} (\rho u (u_r n)) d\Gamma = \int_{\Gamma} (\mathbf{f}_s) d\Gamma + \int_{\Omega} (\rho \mathbf{f_v}) d\Omega \tag{2.10}$$

being f_s the stresses and f_v the volumetric forces.

The application of momentum conservation is only available in layer 1 and layer 2 where there exists velocity. The momentum equation applied to layer 1, Figure 2.6, using Gauss theorem, leads to

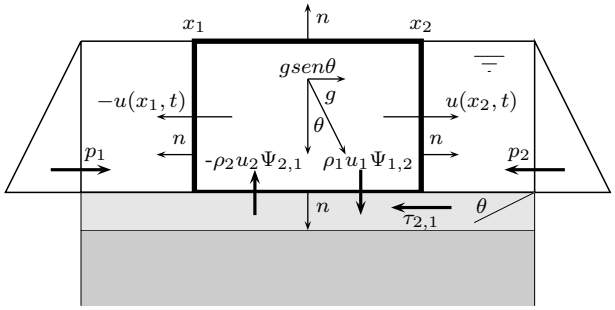

Figure 2.6: Momentum balance in layer 1

$$\underbrace{\frac{d}{dt}\int_{\Omega_1} \rho_1 u_1 d\Omega}_{\textit{Local inertia}} + \underbrace{\int_{\Gamma_1} \rho_1 u_1 u_r n d\Gamma}_{\textit{Convective inertia}} = \underbrace{\int_{\Omega_1} g\rho_1 d\Omega}_{\textit{Gravity force}} + \underbrace{\int_{\Gamma_1} (-pn) d\Gamma}_{\textit{Pressure forces}} + \underbrace{\int_{\Gamma_1} (\tau n) d\Gamma}_{\textit{Tangential forces}} \tag{2.11}$$

where g is the acceleration gravity, p is the pressure (normal stress) and τ is the shear stress.

Expressing (2.11) in differential form:

$$\frac{\partial(h_1\rho_1 u_1)}{\partial t} + \frac{\partial(h_1\rho_1 u_1^2)}{\partial x} + g\frac{\partial\left(\frac{1}{2}\rho_1 h_1^2\right)}{\partial x} + g\frac{\partial(z\rho_1 h_1)}{\partial x} = \\ = (\rho_2 u_2 \Psi_{2,1} - \rho_1 u_1 \Psi_{2,1}) - \tau_{2,1} \tag{2.12}$$

Following the same procedure for layer 2 the corresponding differential form is obtained:

$$\frac{\partial(h_2\rho_2 u_2)}{\partial t} + \frac{\partial(h_2\rho_2 u_2^2)}{\partial x} + g\frac{\partial}{\partial x}\left(\frac{1}{2}\rho_2 h_2^2 + \rho_1 h_1 h_2\right) + g\frac{\partial(z\rho_2 h_2)}{\partial x} = \\ = -(\rho_2 u_2 \Psi_{2,1} - \rho_1 u_1 \Psi_{2,1} + \rho_2 u_2 \Psi_{3,2}) + (\tau_{2,1} - \tau_{2,3}) \tag{2.13}$$

Summary of conservation equations of layers and bed

A summary of the conservation equations obtained from a 1D flow over a mobile bed with a two layer fluid model is provided below

Total mass, layer 1

$$\frac{\partial(\rho_1 h_1)}{\partial t} + \frac{\partial(\rho_1 h_1 u_1)}{\partial x} + \rho_1 \Psi_{2,1}^{net} = 0 \tag{2.14}$$

Total mass, layer 2

$$\frac{\partial \rho_2 h_2}{\partial t} + \frac{\partial(\rho_2 h_2 u_2)}{\partial x} - \rho_2 \Psi_{3,2}^{net} + \rho_2 \Psi_{2,1}^{net} = 0 \tag{2.15}$$

Sediment mass, bed

$$\frac{\partial(\rho_b z \phi_b)}{\partial t} + \rho_b \Psi_{s3,2}^{net} = 0 \tag{2.16}$$

Sediment mass, layer 1

$$\frac{\partial(\rho_1 h_1 \phi_1)}{\partial t} + \frac{\partial(\rho_1 h_1 u_1 \phi_1)}{\partial x} - \rho_1 \Psi_{s2,1}^{net} = 0 \tag{2.17}$$

Sediment mass, layer 2

$$\frac{\partial(\rho_2 h_2 \phi_2)}{\partial t} + \frac{\partial(\rho_2 h_2 u_2 \phi_2)}{\partial x} - \rho_b \Psi_{s3,2}^{net} + \rho_1 \Psi_{s2,1}^{net} = 0 \tag{2.18}$$

Momentum of the mixture, layer 1

$$\frac{\partial(h_1\rho_1 u_1)}{\partial t} + \frac{\partial(h_1\rho_1 u_1^2)}{\partial x} + g\frac{\partial}{\partial x}\left(\frac{1}{2}\rho_1 h_1^2\right) + g\frac{\partial(z\rho_1 h_1)}{\partial x} = \\ = (\rho_2 u_2 \Psi_{2,1} - \rho_1 u_1 \Psi_{2,1}) - \tau_{2,1} \tag{2.19}$$

Momentum of the mixture, layer 2

$$\frac{\partial(h_2\rho_2 u_2)}{\partial t} + \frac{\partial(h_2\rho_2 u_2^2)}{\partial x} + g\frac{\partial}{\partial x}\left(\frac{1}{2}\rho_2 h_2^2 + \rho_1 h_1 h_2\right) + g\frac{\partial(z\rho_2 h_2)}{\partial x} = \\ = -(\rho_2 u_2 \Psi_{2,1} - \rho_1 u_1 \Psi_{2,1} + \rho_2 u_2 \Psi_{3,2}) + (\tau_{2,1} - \tau_{2,3}) \tag{2.20}$$

In case that the granular material is not homogeneous in size or density, the subscript p should be employed to distinguish among cases with non uniform size and specific weight distributions, inside each liquid-granular layer. Thus the formulation becomes:

Total mass, fraction p, layer 1

$$\frac{\partial(\rho_{1p}h_1)}{\partial t} + \frac{\partial(\rho_{1p}h_{1p}u_1)}{\partial x} + \rho_{1p}\Psi^{net}_{2,1} = 0 \tag{2.21}$$

Total mass, fraction p, layer 2

$$\frac{\partial\rho_{2p}h_{2p}}{\partial t} + \frac{\partial(\rho_{2p}h_{2p}u_2)}{\partial x} - \rho_{2p}\Psi^{net}_{3,2} + \rho_{2p}\Psi^{net}_{2,1} = 0 \tag{2.22}$$

Sediment mass, bed

$$\frac{\partial(\rho_b z\phi_b)}{\partial t} + \rho_b\Psi^{net}_{s3,2} = 0 \tag{2.23}$$

Sediment mass, fraction p, layer 1

$$\frac{\partial(\rho_{1p}h_{1p}\phi_{1p})}{\partial t} + \frac{\partial(\rho_{1p}h_{1p}u_1\phi_{1p})}{\partial x} - \rho_{1p}\Psi^{net}_{s2,1} = 0 \tag{2.24}$$

Sediment mass, fraction p, layer 2

$$\frac{\partial(\rho_{2p}h_{2p}\phi_{2p})}{\partial t} + \frac{\partial(\rho_{2p}h_{2p}u_s\phi_{2p})}{\partial x} - \rho_b\Psi^{net}_{s3,2} + \rho_{1p}\Psi^{net}_{s2,1} = 0 \tag{2.25}$$

Momentum of the mixture, layer 1

$$\frac{\partial(h_{1p}\rho_{1p}u_1)}{\partial t} + \frac{\partial(h_{1p}\rho_{1p}u_1^2)}{\partial x} + g\frac{\partial}{\partial x}\left(\frac{1}{2}\rho_{1p}h_{1p}^2\right) + g\frac{\partial(z\rho_{1p}h_{1p})}{\partial x} = \\ = (\rho_{2p}u_2\Psi_{2,1} - \rho_{1p}u_1\Psi_{2,1}) - \tau_{2,1} \tag{2.26}$$

Momentum of the mixture, layer 2

$$\frac{\partial(h_{2p}\rho_{2p}u_2)}{\partial t} + \frac{\partial(h_{2p}\rho_{2p}u_2^2)}{\partial x} + g\frac{\partial}{\partial x}\left(\frac{1}{2}\rho_{2p}h_{2p}^2 + \rho_{1p}h_{1p}h_{2p}\right) + g\frac{\partial(z\rho_{2p}h_{2p})}{\partial x} = \\ = -(\rho_{2p}u_2\Psi_{2,1} - \rho_{1p}u_1\Psi_{2,1} + \rho_{2p}u_2\Psi_{3,2}) + (\tau_{2,1} - \tau_{2,3}) \tag{2.27}$$

There are $(5+2)N_p$ equations, being N_p the number of size fractions p which had the bed material, and $(5+2)N_p$ independent variables: the flow depth for each layer, h_{1p}, h_{2p}; the depth averaged velocity in layer 1, u_1 and in layer 2, u_2; the bottom elevation, z and finally the sediment concentration in layer 1 of fraction p, ϕ_{1p} and in layer 2, ϕ_{2p}.

Several closure equations are required to express the shear stress between layers, $\tau_{2,1}$ and $\tau_{2,3}$ and the sediment fluxes, $\Psi_{2,1}$ and $\Psi_{3,2}$ in terms of the independent variables. This represents such a complex task that it justifies further simplification of the model. Next section is devoted to discuss this.

2.3 One layer model

The one layer model, Figure (2.7), is built upon a set of assumptions in relation to the two layer model: (i) a unique layer of depth h is considered, which includes previous layer 1 and 2, (ii) continuity approach, assuming the same velocity for the liquid and for the solid phase, u, which leads to continuity of momentum and consequently to a continuity of shear stresses, avoiding the necessity of calculating τ_{ij} between interfaces.

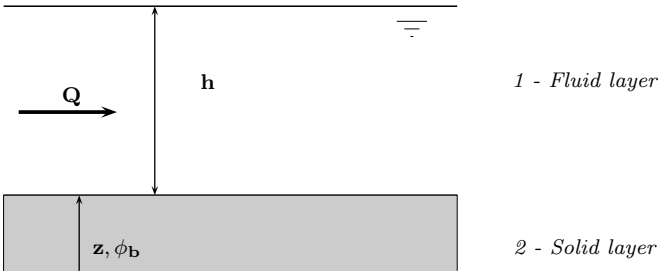

Figure 2.7: Interfaces in the domain

2.3.1 Conservation equations

The relevant formulation of the model derives from the depth-averaged equation of bulk mass conservation, mixture momentum conservation and conservation of the mass of the different constituents.

The term ϕ_p represents the scalar depth-averaged volumetric concentration of component p, with $p = 1, ..., N_p$ and N_p the number of different components transported. The mixture density is given by $\rho_m = \rho_w r$ where ρ_w is the density of the water and r means the relative density of the bulk mixture with respect the clean water

$$r = 1 + \sum_{p=1}^{N_p} \Delta_p \phi_p \tag{2.28}$$

where $\Delta_p = (\rho_p - \rho_w)/\rho_w$ is the relative density of the solid phase p. It is assumed that dissolved species with low concentration do not change bulk density $\Delta_p = 0$. In case of having an unique specie the relative density of the bulk mixture becomes $r = 1 + \Delta\phi$.

Mass conservation

Considering a generic control volume for a horizontal flow over a mobile bed where the velocity is depth averaged, defined in Figure 2.7, the Reynolds transport for mass conservation at the liquid layer leads to:

$$\int_{x_1}^{x_2} \frac{\partial}{\partial t}(\rho_m h)dx + \int_{x_1}^{x_2} \frac{\partial}{\partial x}(\rho_m hu)dx + \int_{x_1}^{x_2} \rho_m \Psi_s^{net} dx = 0 \tag{2.29}$$

and to the sediment balance mass

$$\int_{x_1}^{x_2} \frac{\partial}{\partial t}(h \sum_{p=1}^{N_p} \rho_p \phi_p)dx + \int_{x_1}^{x_2} \frac{\partial}{\partial x}(hu \sum_{p=1}^{N_p} \rho_p \phi_p)dx + \int_{x_1}^{x_2} \sum_{p=1}^{N_p} \rho_p \Psi_p^{net} dx = 0 \tag{2.30}$$

Following the same procedure for mass sediment balance at the bottom and considering, $\phi_{b_p} = (1 - p_p)$, being p_p the porosity of each sediment, drives to

$$\int_{x_1}^{x_2} \frac{\partial}{\partial t}(z \sum_{p=1}^{N_p} \rho_p(1 - p_p))dx - \int_{x_1}^{x_2} \sum_{p=1}^{N_p} \rho_p \Psi_p^{net} dx = 0 \tag{2.31}$$

The term Ψ_s^{net}, which appears in the above set of equations, includes the vertical sediment flux, suspension transport, and the horizontal sediment flux, bed load transport.

$$\Psi_s^{net} = \Psi_{load} + \Psi_{susp} \tag{2.32}$$

Momentum equation

For the x direction, and considering Figure 2.7, the momentum conservation equation for the mixing layer, which is the unique zone where there exists velocity, and with the x component of the gravity mass force equal to 0, $(\mathbf{f_v})_x = 0$, leads to

$$\int_{x_1}^{x_2} \frac{\partial}{\partial t}(\rho_m hu)dx + \int_{x_1}^{x_2} \frac{\partial}{\partial x}(\rho_m hu^2)dx = \int_{x_1}^{x_2} p_b dx - \int_{x_1}^{x_2} \tau_b dx \tag{2.33}$$

The term of superficial forces, $(\mathbf{f_s})_x$, has been split in its two components, the hydrostatic pressure, p_b, and the friction term exerted over the bed, τ_b.

$$\mathbf{f_s} = p_b - \tau_b \tag{2.34}$$

Summary of conservation equations

The set of developed differential equations is newly written below in terms of the relative density r.

Total mass

$$\frac{\partial(hr)}{\partial t} + \frac{\partial(hur)}{\partial x} = \sum_{p=1}^{N_p} \Delta\Psi_p^{net} \tag{2.35}$$

Sediment mass, bed

$$\frac{\partial(z)}{\partial t} + \sum_{p=1}^{N_p} \frac{\Psi_p^{net}}{(1 - p_p)} = 0 \tag{2.36}$$

Sediment mass of the mixing layer for specie p

$$\frac{\partial(h\phi_p)}{\partial t} + \frac{\partial(hu\phi_p)}{\partial x} = \Psi_p^{net} \tag{2.37}$$

Momentum of the mixing layer

$$\frac{\partial(hur)}{\partial t} + \frac{\partial[hu^2r + (1/2)gh^2r]}{\partial x} = \frac{p_b}{\rho_w} - \frac{\tau_b}{\rho_w} \tag{2.38}$$

There are $3+N_p$ equations and $3+N_p$ variables, being N_p the number of species: the flow depth, h, the mean flow velocity, u, the bed level, z, and the depth averaged sediment concentration, ϕ_p. Furthermore two closure equations are still needed, one for the bed shear stress, τ_b, and another one for the formulation of the sediment flux between flow and bed, Ψ_p^{net}. In the search for the simplest model involving the minimum number of closure relations, the above formulation can be transformed into Exner equation, next presented.

2.3.2 Exner equation

The above set of equations may be manipulated leading to a simpler model. Inserting Ψ_p from (2.36) in (2.37) leads to the following sediment mass conservation,

$$\frac{\partial z}{\partial t} + \frac{1}{(1-p_p)}\frac{\partial(hu\phi_p)}{\partial x} = -\frac{1}{(1-p_p)}\frac{\partial(h\phi_p)}{\partial t} \tag{2.39}$$

The second term on the left hand side of (2.39) is the derivative of transported sediment flow $q_{s,x} = hu\phi_p$ along the x coordinate, whereas the term on the right side contains information about the temporal evolution of the bed level due to vertical fluxes of material in cases of suspended material. They become the Exner equation (Kalinske, 1947), expressed as follows

$$\frac{\partial z}{\partial t} + \xi\frac{\partial q_{s,x}}{\partial x} = \xi\omega_s\left(E_s - c_b\right) \tag{2.40}$$

with $\xi = \frac{1}{1-p_p}$, ω_s the settling velocity of the sediment particles, E_s a dimensionless factor accounting for the sediment material entering the volume by suspension and ϕ_b is the suspended material concentration. Both terms of $q_{s,x}$ and $\xi\omega_s\left(E_s - \phi_b\right)$ can be estimated if using empirical closure formulae, that depend on the flow conditions.

Regarding the bulk density, it can be evaluated assuming that the volumetric concentration is given by the closure formulae themselves (Rosatti *et al.*, 2007). In many environmental problems, the bulk density remains almost constant and furthermore low concentrations of transported material are present. This means that further simplications over liquid phase mass and momentum conservation equations are admissible, allowing the elimination of the dependence with the relative density of the mixture, r. Alternatively, assuming that the sediment material presents low concentration and does not change the bulk density, the relative density of the mixture, r can be made constant and equal to 1.

Gathering the depth averaged set of equations which governed the 1D flow and the sediment dynamics leads to

Mass

$$\frac{\partial(h)}{\partial t} + \frac{\partial(hu)}{\partial x} = 0 \tag{2.41}$$

Momentum

$$\frac{\partial(hu)}{\partial t} + \frac{\partial[hu^2 + (1/2)gh^2]}{\partial x} = \frac{p_b}{\rho_w} - \frac{\tau_b}{\rho_w} \tag{2.42}$$

Sediment mass, bed

$$\frac{\partial z}{\partial t} + \xi \frac{\partial q_{s,x}}{\partial x} = \xi \omega_s \left(E_s - c_b\right) \tag{2.43}$$

The extension of the formulation of the shallow water equations to unsteady 2D flow over mobile bed using the Exner equation approach is:

Mass

$$\frac{\partial(h)}{\partial t} + \frac{\partial(hu)}{\partial x} + \frac{\partial(hv)}{\partial y} = 0 \tag{2.44}$$

Momentum in x direction

$$\frac{\partial(hu)}{\partial t} + \frac{\partial[hu^2 + (1/2)gh^2]}{\partial x} + \frac{\partial(huv)}{\partial y} = \frac{p_{bx}}{\rho_w} - \frac{\tau_{bx}}{\rho_w} \tag{2.45}$$

Momentum in y direction

$$\frac{\partial(hu)}{\partial t} + \frac{\partial(huv)}{\partial x} + \frac{\partial[hv^2 + (1/2)gh^2]}{\partial y} = \frac{p_{by}}{\rho_w} - \frac{\tau_{by}}{\rho_w} \tag{2.46}$$

Sediment mass, bed

$$\frac{\partial z}{\partial t} + \xi \frac{\partial q_{s,x}}{\partial x} + \xi \frac{\partial q_{s,y}}{\partial y} = \xi \omega_s \left(E_s - c_b\right) \tag{2.47}$$

with (u, v) the depth averaged components of the velocity vector along the (x, y) coordinates.

The above set of equations have been used to study the relative behavior of the sediment transport capacity formulae described in the next chapter.

Chapter 3

Bed load formulation

3.1 Introduction

When using the Exner equation, horizontal solid fluxes can be evaluated using capacity formulae. In this chapter, different formulations empirically proposed for the modeling of non-cohesive granular material flows are presented and written following a unified expression. In this work mass exchange fluxes associated to suspended load will be considered negligible in comparison with bed load transport, and therefore will not be included in the mathematical model.

3.2 Description of bed load formulation

Considering a bidimensional flow where the solid transport is focused on the bed load, the Exner equation can be written as

$$\frac{\partial z}{\partial t} + \xi \frac{\partial q_{s,x}}{\partial x} + \xi \frac{\partial q_{s,y}}{\partial y} = 0 \tag{3.1}$$

The formulation of the bed load discharge q_s can be based on deterministic laws (Meyer-Peter & Müller, 1948), (Camenen & Larson, 2005), (Smart, 1984) or in probabilistic methods (Kalinske, 1947), (Einstein, 1950), always supported by experimentation. Grass (Grass, 1981) discussed one of the most basic sediment transport laws that in 2D can be written as (Hudson, 2001)

$$q_{s,x} = A_g u \left(u^2 + v^2\right) \qquad q_{s,y} = A_g v \left(u^2 + v^2\right) \tag{3.2}$$

This deterministic formulation is well suited for the modeling of non-cohesive granular material and, as a basic feature, this model does not involve any sediment movement threshold but assumes that the flow is always able to mobilize the bed. The model requires a dimensional calibration constant A_g, accounting for the effects associated to

the grain size and the kinematic viscosity. Ranging typically from 0 to 1, it represents a stronger interaction between flow and sediment as it approaches 1.

Following the idea presented in (Murillo & García-Navarro, 2010), A_g can be determined by using the empirical deterministic formulae avoiding the necessity of expressing this quantity as a calibration constant in each particular problem. To do this, several empirical formulations for sediment transport will be analyzed assuming that it is possible to write them all as

$$A_g = A_g(h, q_{s,x}, q_{s,y}) \tag{3.3}$$

The bed load transport is often represented by the following dimensionless parameter,

$$\Phi = \frac{|\mathbf{q}_s|}{\sqrt{g(s-1)d_m^3}} \tag{3.4}$$

where $s = \rho_p/\rho_w$ is the ratio between solid material (ρ_p) and water densities, and d_m is the median diameter.

The dimensionless bottom shear stress or Shields parameter, can be expressed as:

$$\theta = \frac{|\mathbf{T}_b|}{g(\rho_s - \rho_w)d_m} \tag{3.5}$$

where $\mathbf{T}_b = (\tau_{b,x}, \tau_{b,y})$ is the shear stress at the bottom due to the steady flow, that written in terms of the Manning-Strickler's coefficient (3.6) can be expressed as

$$\begin{array}{ll} \frac{\tau_{b,x}}{\rho_w} = ghS_{f,x} & S_{f,x} = \frac{n^2 u\sqrt{u^2+v^2}}{h^{4/3}} \\ \frac{\tau_{b,y}}{\rho_w} = ghS_{f,y} & S_{f,y} = \frac{n^2 v\sqrt{u^2+v^2}}{h^{4/3}} \end{array} \tag{3.6}$$

This allows to express $|\mathbf{T}_b|$ as

$$|\mathbf{T}_b| = \sqrt{\tau_{b,x}^2 + \tau_{b,y}^2} = \sqrt{(\rho_w ghS_{f,x})^2 + (\rho_w ghS_{f,y})^2} \tag{3.7}$$

leading to the following expression for the Shields parameter:

$$\theta = \frac{n^2}{(s-1)d_m h^{1/3}}(u^2+v^2) = \frac{n^2}{(s-1)d_m h^{1/3}}|\mathbf{u}|^2 \tag{3.8}$$

Different commonly applied empirical deterministic formulae are written in terms of Φ and θ. The formulae tested in this work are gathered in Table 3.1, where d_{90} and d_{30} are the grain diameter for which 90% and 30% of the weight of a nonuniform sample is finer respectively, C is the flow resistance factor $C = u/(ghS_f)^{0.5}$, S_o is the bed slope, θ_c is the critical Shields parameter, Table 3.2, expressing the sediment movement threshold, and

Table 3.1: Summary of sediment formulae

Formula	Φ
Meyer-Peter & Müller (1948)	$8\ (\theta-\theta_c)^{3/2}$
Ashida & Michiue (1972)	$17\ (\theta-\theta_c)(\sqrt{\theta}-\sqrt{\theta_c})$
Engelund & Fredsoe (1976)	$18.74\ (\theta-\theta_c)(\sqrt{\theta}-0.7\sqrt{\theta_c})$
Luque & van Beek (1976)	$5.7\ (\theta-\theta_c)^{3/2}$
Parker (1979) fit to Einstein (1950)	$11.2\ \theta^{3/2}\,(1-\theta/\theta_c)^{9/2}$
Smart (1984)	$4\ (d_{90}/d_{30})^{0.2}\ S_o^{0.6}\ C\theta^{1/2}(\theta-\theta_c^S)$
Nielsen (1992)	$12\ \theta^{1/2}(\theta-\theta_c)$
Wong (2003)	$4.93\ (\theta-\theta_c)^{1.6}$
Wong (2003)	$3.97\ (\theta-\theta_c)^{3/2}$
Camenen & Larson (2005)	$12\ \theta^{3/2}\exp(-\theta/\theta_c)$

Table 3.2: Summary of threshold of non dimensional shear stress

Formula	θ_c
Meyer-Peter and Müller (1948)	0.0470
Ashida and Michiue (1972)	0.0500
Engelund and Fredsoe (1976)	0.0500
Fernandez Luque and Van Beek (1976)	0.037–0.0455
Parker (1979) fit to Einstein (1950)	0.030
Smart(1984)	0.0470
Nielsen (1992)	0.0470
Wong (2003)	0.0470
Wong (2003)	0.0495
Camenen and Larson(2005)	0.0400

$$\theta_c^S = \theta_c \cos\phi \left(1 - \frac{\tan\phi}{\tan\psi}\right) \tag{3.9}$$

with ϕ the angle of the bed slope and ψ the angle of repose of saturated bed material. Using (3.8) and (3.4) the transport formulae in (3.1) can be expressed as

$$|\mathbf{q}_s| = K_0\ K_1\ (u^2+v^2)^{3/2} = A_g|\mathbf{u}|^3 \tag{3.10}$$

with $A_g = K_0\ K_1$, $K_0 = \frac{g^{1/2}n^3}{(s-1)h^{1/2}}$ and K_1 varying in each case as displayed in Table 3.3.

Table 3.3: Summary of Grass coefficients written for sediment formulae

Formula	K_1
Meyer-Peter and Müller (1948)	$8\,(1-\theta_c/\theta)^{3/2}$
Ashida and Michiue (1972)	$17\,(1-\theta_c/\theta)(1-\sqrt{\theta_c/\theta})$
Engelund and Fredsoe (1976)	$18.74\,(1-\theta_c/\theta)(1-0.7\sqrt{\theta_c/\theta})$
Fernandez Luque and Van Beek (1976)	$5.7\,(1-\theta_c/\theta)^{3/2}$
Parker (1979) fit to Einstein (1950)	$11.2\ (1-\theta/\theta_c)^{9/2}$
Smart(1984)	$4\ (d_{90}/d_{30})^{0.2}\ S_o^{0.6}\,C\,(1-\theta_c/\theta)$
Nielsen (1992)	$12\,(1-\theta_c/\theta)$
Wong (2003)	$4.93\,(1-\theta_c/\theta)^{3/2}\,(\theta-\theta_c)^{0.1}$
Wong (2003)	$3.97\,(1-\theta_c/\theta)^{3/2}$
Camenen and Larson(2005)	$12\ \exp(-\theta/\theta_c)$

These more complex definitions provided for A_g, (3.10), allows to standardize sediment transport formulae and perform a study about their relative behavior under different hydrodynamic and morphodynamic conditions.

Chapter 4

Numerical scheme

4.1 Introduction

In order to build a well suited bed load model for unsteady flow, the previous system of equations presented in the one layer model for the shallow water (2.41) and for the Exner model (2.40) is written in a 2D coupled form as follows:

$$\frac{\partial \mathbf{U}}{\partial t} + \frac{\partial \mathbf{F}(\mathbf{U})}{\partial x} + \frac{\partial \mathbf{G}(\mathbf{U})}{\partial y} = \mathbf{S}(\mathbf{U}, x, y) \tag{4.1}$$

where

$$\mathbf{U} = (h,\ q_x,\ q_y,\ z)^T \tag{4.2}$$

with

$$\begin{aligned} \mathbf{F} &= \left(q_x,\ \tfrac{q_x^2}{h} + \tfrac{1}{2}gh^2,\ \tfrac{q_x q_y}{h},\ A_g \tfrac{q_x(q_x^2+q_y^2)}{h^3}\right)^T \\ \mathbf{G} &= \left(q_y,\ \tfrac{q_x q_y}{h},\ \tfrac{q_y^2}{h} + \tfrac{1}{2}gh^2,\ A_g \tfrac{q_y(q_x^2+q_y^2)}{h^3}\right)^T \end{aligned} \tag{4.3}$$

and the source term $\mathbf{S}$

$$\mathbf{S} = \left(0,\ \frac{p_{b,x}}{\rho_w} - \frac{\tau_{b,x}}{\rho_w},\ \frac{p_{b,y}}{\rho_w} - \frac{\tau_{b,y}}{\rho_w},\ 0\right)^T \tag{4.4}$$

In the next section, the finite volume scheme is described.

4.2 Description of the finite volume scheme

To introduce the finite volume scheme, (4.1) is integrated in a constant size volume or grid cell Ω using Gauss theorem:

$$\frac{\partial}{\partial t}\int_{\Omega}\mathbf{U}d\Omega+\oint_{\partial\Omega}\mathbf{E_n}dl=\int_{\Omega}\mathbf{S}d\Omega \tag{4.5}$$

where $\mathbf{E_n}=\mathbf{F}n_x+\mathbf{G}n_y$ and $\mathbf{n}=(n_x,n_y)$ is the outward unit normal vector to the volume Ω. In order to obtain a numerical solution of system (4.1) we divide the domain in computational cells, Ω_i, using a mesh fixed in time, and (4.5) is applied to each cell

$$\frac{\partial}{\partial t}\int_{\Omega_i}\mathbf{U}d\Omega+\sum_{k=1}^{NE}\int(\mathbf{E_n})_k^{\downarrow}dl_k=\int_{\Omega_i}\mathbf{S}d\Omega \tag{4.6}$$

Here $(\mathbf{E_n})_k^{\downarrow}$ is the value of the interface flux function through the edge k to be defined, $\mathbf{n}_k=(n_x,n_y)$ is the outward unit normal vector to the cell edge k, and NE is the number of edges in cell i. Assuming a piecewise representation per cell of the conserved variables,

$$\mathbf{U}_i^n=\frac{1}{A_i}\int_{\Omega_i}\mathbf{U}(x,y,t^n)d\Omega \tag{4.7}$$

(4.6) is written as

$$\frac{\partial}{\partial t}\int_{\Omega_i}\mathbf{U}d\Omega+\sum_{k=1}^{NE}(\mathbf{E_n})_k^{\downarrow}l_k=\sum_{k=1}^{NE}\mathbf{T}_{\mathbf{n},b}l_k+\sum_{k=1}^{NE}\mathbf{T}_{\mathbf{n},s}l_k \tag{4.8}$$

where l_k is the corresponding edge length and $\mathbf{T}_b\mathbf{n}$ and $\mathbf{T}_s\mathbf{n}$ are suitable integrals of the bed slope and friction source terms (Murillo *et al.*, 2009):

$$(\mathbf{T}_{\mathbf{n},b})_k=\left(\frac{p_b}{\rho_w}\right)_k\left(\ 0,n_x,n_y\ \right)_k^T\quad(\mathbf{T}_{\mathbf{n},s})_k=g(\widetilde{h}S_f)_k d_{\mathbf{n}}\left(\ 0,n_x,n_y\ \right)_k^T \tag{4.9}$$

with $\widetilde{h}=1/2(h_i+h_j)$, i and j the cells sharing edge k, $S_{f,k}$ the friction slope and $d_{\mathbf{n}}$ the normal distance between neighboring cell centers.

The numerical scheme is constructed by defining an approximate Jacobian matrix $\widetilde{\mathbf{J}}$ at each k edge each cell combining the normal flux $\mathbf{E_n}$ with the bed slope source term $\mathbf{T}_{\mathbf{n},b}$ at each cell edge

$$(\delta\mathbf{E}-\mathbf{T_b})_{k\mathbf{n}_k}=\widetilde{\mathbf{J}}_{\mathbf{n},k}\delta\mathbf{U}_k \tag{4.10}$$

with $\delta(\mathbf{E_n})_k=(\mathbf{E}_j-\mathbf{E}_i)_{\mathbf{n}_k}$, $\delta\mathbf{U}_k=\mathbf{U}_j-\mathbf{U}_i$, and $\mathbf{U}_i$ and $\mathbf{U}_j$ the initial values at cells i and j sharing edge k. The approximate Jacobian matrix $\widetilde{\mathbf{J}}$ is

$$\widetilde{\mathbf{J}}_{\mathbf{n},k} = \begin{pmatrix} 0 & n_x & n_y & 0 \\ (\widetilde{c}^2 - \widetilde{u}^2)n_x - \widetilde{u}\widetilde{v}n_y & 2\widetilde{u}n_x + \widetilde{v}n_y & \widetilde{u}n_y & p_{bz}n_x \\ -\widetilde{u}\widetilde{v}n_x + (\widetilde{c}^2 - \widetilde{v}^2)n_y & \widetilde{v}n_x & \widetilde{u}n_x + 2\widetilde{v}n_y & p_{bz}n_y \\ \widetilde{A} & \widetilde{B} & \widetilde{C} & 0 \end{pmatrix} \tag{4.11}$$

being $\widetilde{u}$, $\widetilde{v}$ and $\widetilde{c}$ the Roe averaged variables (Roe, 1986)

$$\widetilde{u} = \frac{u_i\sqrt{h_i} + u_j\sqrt{h_j}}{\sqrt{h_i} + \sqrt{h_j}}, \qquad \widetilde{v} = \frac{v_i\sqrt{h_i} + v_j\sqrt{h_j}}{\sqrt{h_i} + \sqrt{h_j}}, \qquad \widetilde{c} = \sqrt{g\frac{h_i + h_j}{2}} \tag{4.12}$$

and the coefficients $\widetilde{A}$, $\widetilde{B}$ and $\widetilde{C}$ equal to

$$\begin{aligned} \widetilde{A} &= -(C_1 n_x + C_2 n_y)\widetilde{u} - (C_2 n_x + C_3 n_y)\widetilde{v} \\ \widetilde{B} &= (C_1 n_x + C_2 n_y) \\ \widetilde{C} &= (C_2 n_x + C_3 n_y) \end{aligned} \tag{4.13}$$

where

$$\begin{aligned} C_1 &= A_{g,k}\,\xi\frac{(u_i^2 + u_i u_j + u_j^2)}{\sqrt{h_i h_j}} + A_{g,k}\,\xi\frac{v_i v_j}{\sqrt{h_i h_j}} \\ C_2 &= A_{g,k}\,\xi\frac{(u_i v_i + u_j v_j)}{\sqrt{h_i h_j}} \\ C_3 &= A_{g,k}\,\xi\frac{(v_i^2 + v_i v_j + v_j^2)}{\sqrt{h_i h_j}} + A_{g,k}\,\xi\frac{u_i u_j}{\sqrt{h_i h_j}} \end{aligned} \tag{4.14}$$

As the coefficient A_g is not a constant but varies from cell to cell, at every edge k a local $A_{g,k}$ value is defined as an arithmetic mean between cells

$$A_{g,k} = \frac{A_{g,i} + A_{g,j}}{2} \tag{4.15}$$

where the $A_{g,i}$ coefficients are obtained through the relations presented in the bed load formulation chapter. Other average possibilities have been tested leading to negligible differences.

From the approximate Jacobian matrix in (4.11) a set of four real eigenvalues $\widetilde{\lambda}_k^m$ and eigenvectors $\widetilde{\mathbf{e}}_k^m$ are obtained (see Appendix A for their detailed expression). Vector $\mathbf{U}$ is then split through the matrix eigenvectors basis, $\widetilde{\mathbf{P}}$, as

$$\delta\mathbf{U}_k = \widetilde{\mathbf{P}}_k\mathbf{A}_k \tag{4.16}$$

with

$$\widetilde{\mathbf{P}_k} = (\widetilde{\mathbf{e}}^1, \widetilde{\mathbf{e}}^2, \widetilde{\mathbf{e}}^3, \widetilde{\mathbf{e}}^4) \qquad \mathbf{A}_k = \begin{pmatrix} \alpha^1 & \alpha^2 & \alpha^3 & \alpha^4 \end{pmatrix}_k^T \tag{4.17}$$

The friction source terms are also projected onto the matrix eigenvectors basis, $\widetilde{\mathbf{P}}$, in 4.18, to guarantee the exact equilibrium between fluxes and source terms

$$(\mathbf{T_{n},}_{s})_k = \widetilde{\mathbf{P}}_k \mathbf{B}_k \tag{4.18}$$

with

$$\mathbf{B}_k = \begin{pmatrix} \beta^1 & \beta^2 & \beta^3 & \beta^4 \end{pmatrix}_k^T \tag{4.19}$$

The complete details of the coefficients can be found in (Murillo & García-Navarro, 2010). Gathering all the previous information the volume integral in the cell at time t^{n+1} is expressed as

$$\mathbf{U}_i^{n+1} = \mathbf{U}_i^n - \sum_{k=1}^{NE} \sum_{m=1}^{4} (\widetilde{\lambda}^- \alpha - \beta^-)_k^m \widetilde{\mathbf{e}}_{JI,k}^m l_k \frac{\Delta t}{A_i} - \sum_{k=1}^{NE} \delta \mathbf{E}_{Ii,k} \mathbf{n}_k l_k \frac{\Delta t}{A_i} \tag{4.20}$$

being l_k the length of the edge normal to the n_k vector and

$$\widetilde{\beta}_k^{\pm,m} = \frac{1}{2}(1 \pm sign(\widetilde{\lambda}))_k^m \beta_k^m \qquad \widetilde{\lambda}_k^{\pm,m} = \frac{1}{2}(\widetilde{\lambda} \pm |\widetilde{\lambda}|)_k^m \tag{4.21}$$

in (4.20) the second term of the right side evaluates the flux in the cell edge and the third term completes the updating formula to consider the spacial variation of A_g, see Appendix B for further details.

The updated value $\mathbf{U}_i^{n+1}$ in (4.20) can be interpreted as a cell average of the contributions of the local RPs, and in consequence the time step Δt is taken small enough so that there is no interaction of waves from the k neighboring Riemann problems. In the 2D framework, considering unstructured meshes, the relevant distance, that will be referred to as χ_i in each cell i must consider the volume of the cell and the length of the shared k edges (Murillo & García-Navarro, 2010),

$$\chi_i = \frac{A_i}{\max_{k=1,NE} l_k} \tag{4.22}$$

Considering that each k RP is used to deliver information to a pair of neighboring cells of different size, the distance $\min(A_i, A_j)/l_k$ is relevant, so in case that the water depth is greater than zero in all the regions of the RP solution the time step is limited by

$$\Delta t \leq CFL\ \Delta t^{\widetilde{\lambda}} \qquad \Delta t^{\widetilde{\lambda}} = \frac{\min(\chi_i, \chi_j)}{\max |\widetilde{\lambda}^m|} \tag{4.23}$$

with CFL=1/2 in the case of rectangular or structured triangular cells and, according to computational experience, CFL close to 1 for triangular unstructured grids as the construction of finite volume schemes from direct application of one-dimensional fluxes leads to reduced stability ranges (Toro, 2001).

4.2.1 Numerical discretization of the bed slope in the generalized Grass coefficient for the Smart formulation

Empirical formulations for bed load transport presented in the previous chapter are written as a function of the bed friction slope, except in the case of the Smart formulation, that considers an additional term based on an estimation of the bed slope along the preferential flow direction.

$$\Phi = 4\ (d_{90}/d_{30})^{0.2}\ S_o^{0.6}\ C\theta^{1/2}(\theta - \theta_c^S) \tag{4.24}$$

where Φ is the dimensionless sediment transport, θ is the dimensionless shear stress, d_{90} and d_{30} are the grain diameters for which 90% and 30% of the weight of a non-uniform sample is finer respectively, S_o stands for the bed slope along the preferential flow direction, θ_c is the critical Shields parameter, and C is the flow resistance factor $C = u/(ghS_f)^{0.5}$, being u the unique velocity in the 1D experimental tests carried out by Smart and S_f the friction slope along that direction, calculated as 3.6.

In a 2D model both the bed slope and friction slope are defined along the two horizontal coordinate directions. This subsection is devoted to the discussion of their correct evaluation in that case. As the Smart formula was derived from 1D experimental cases involving the bed slope in the flow direction, in 2D simulation it is necessary to evaluate the bed slope in the local flow direction, $|S_{o,\mathbf{u}}|$. The bed slope in the flow direction is given by:

$$|S_{o,\mathbf{u}}|_i = |\mathbf{S}_{o,i}\mathbf{n}_{\mathbf{u},i}| \tag{4.25}$$

where $\mathbf{n}_{\mathbf{u},i}$ is the unit vector associated to the local velocity $\mathbf{u}, i$ at each cell i. As in 2D the bed level surface is defined by a plane, the following technique, able to handle both rectangular and triangular meshes, is used to evaluate the bed slope $\mathbf{S}_{o,i} = (S_{o,x}, S_{o,y})$ in each cell (Murillo *et al.*, 2009),

$$S_{o,x} = \left(\sum_{k=1}^{NE}\left(\frac{\delta z\, n_x}{d_{\mathbf{n}}}\right)\right)\left(\sum_{k=1}^{NE}|n_x|\right)^{-1} \quad S_{o,y} = \left(\sum_{k=1}^{NE}\left(\frac{\delta z\, n_y}{d_{\mathbf{n}}}\right)\right)\left(\sum_{k=1}^{NE}|n_y|\right)^{-1} \tag{4.26}$$

where δz is the difference of bottom heights, d_n is the normal distance between the centers of cells and n_x, n_y are the components of the normal vector along the axis.

Furthermore, in cases where the flow finds a nil or an adverse slope $\mathbf{S}_{o,i}\mathbf{u}_i \leq 0$ the bed slope in (4.25) is replaced by the friction slope computed in cell i, $\mathbf{S}_{f,i}$, with the components as defined in (3.6) . This option will be referred to as Smart CFBS (Combined Friction and Bed Slope). In case of using under any morphodynamic condition the friction slope, the option will be called Smart.

Chapter 5

One dimensional cases

5.1 Introduction

This chapter gathers 1D cases with experimental data in order to study the relative behavior of the numerical results predicted when using different sediment transport formulae. These closure laws were derived from 1D experimental steady flows and are going to be tested in order to verify their capacity of prediction in unsteady situations.

First, a series of sudden dam break test cases are presented, with a combination of morphodynamic and hydrodynamic situations. In the next test case, dam erosion in time due to flow overtopping is considered. In all these numerical experiments the flow finds different regions under subcritical or supercritical regime. The last experiment considers a case of fully subcritical flow, with an important discontinuity at the bottom.

5.2 Dam break test cases

These experiments were performed in a flume designed at the UCL Civil Engineering Department (Spinewine & Zech, 2007). The flume had a length of 6 m, 3 m on both sides of a central gate simulating an idealized dam. The channel width was set constant and equal to 25 cm. The bed material was uniform coarse sand with the following properties: particle sizes ranging from 1.2 to 2.4 mm, with $d_{50} = 1.82$ mm, density $\rho_s = 2683$ kg m^{-3}, a friction angle $\varphi = 30^o$, negligible cohesion, porosity $p = 0.47$ and was characterized by a Manning roughness factor $n = 0.0165$ sm$^{-1/3}$.

Table 5.1 summarizes the set of experiments selected in this work. The regions upstream and downstream the gate were filled with sediments and different water depths. The three first test cases, A, B, and D, have been chosen to guarantee the correct performance of the numerical scheme in combination with a discharge formulation, in cases where morphological changes are produced in presence of dry bed and null, adverse or in favorable slope. Case F allows checking if the numerical scheme in combination with a discharge formulation is able to handle with the different type of waves that may arise in a dam break case over wet bed. Numerical simulations have been performed

Table 5.1: Summary of dam break test cases.

Test	h_L	h_R	z_L	z_R
A	0.35	0.00	0.00	0.00
B	0.40	0.00	-0.05	0.00
D	0.25	0.00	0.10	0.00
F	0.25	0.10	0.10	0.00

using $\Delta x = 0.01$ m and CFL = 1.0. In all the simulations the bed domain is considered deformable and no boundary condition is imposed at the downstream section.

5.2.1 Test A

Test A is a dam break over dry bed with an initially plain bed level. The flow evolves in time leading to a left moving rarefaction wave upstream the gate ending in a flooding front dominated by friction. The experimental results are close to those ones obtained for dam break cases over dry and fixed bed Dressler (1954). Figure 5.1 shows the numerical results and experimental data for the dam break test case A using MPM (left) and Smart CFBS (right). In this case little scour is produced and both formulations provide indistinguishable results. The Smart CFBS formulation provides a correct tracking of the advance velocity, bed level and water level surface in time, as shown in Figure 5.2. Considering that the numerical scheme is conservative, differences among measured and computational data are expected to be produced by the lack of an infiltration parameter in the numerical model.

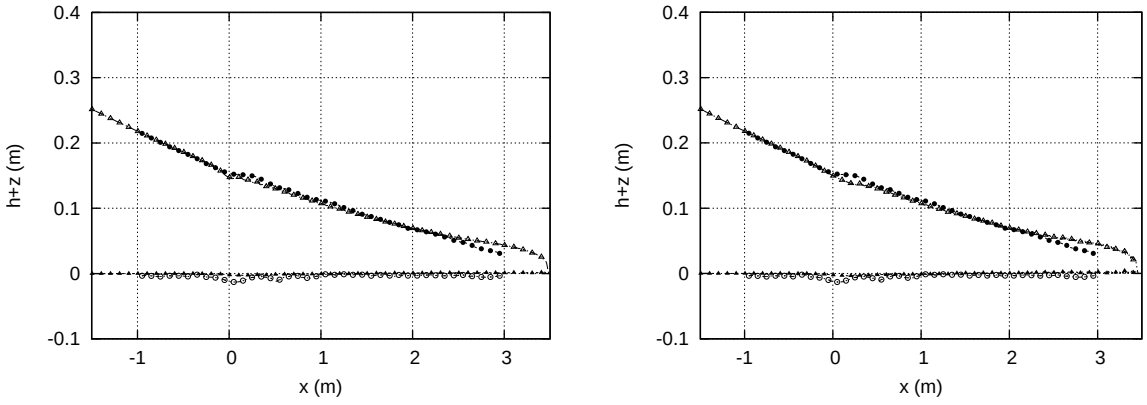

Figure 5.1: Numerical results and experimental data for the dam break test case A at $t = 1.5$ s, using a variable value of A_g computed using MPM (left) and Smart CFBS (right): measured water level surface ($-\bullet-$), measured bed level surface ($-\circ-$), computed water level surface ($-\triangle-$), computed bed level surface ($-\blacktriangle-$)

In Figure 5.2 numerical results and experimental data have been plotted for test case A, for times ranging from 0 to 1.5 seconds. The front wave is numerically well reproduced in space and time when using Smart CFBS.

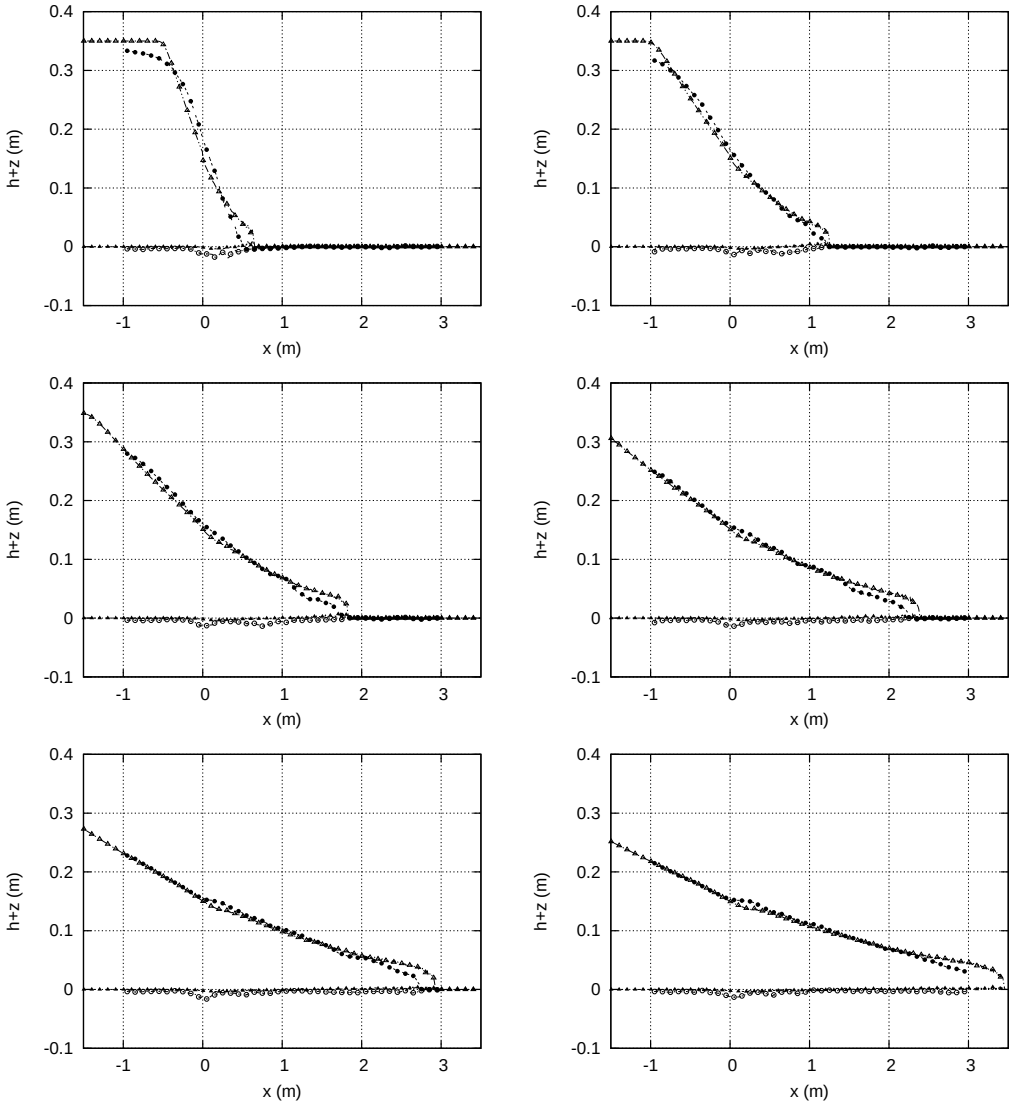

Figure 5.2: Numerical results and experimental data for the dam break test case A at times $t = 0.025$, 0.050, 0.075, 0.100, 0.125 and 1.5 s, using a variable value of A_g computed using Smart CFBS: measured water level surface ($-\bullet-$), measured bed level surface ($-\circ-$), computed water level surface ($-\triangle-$), computed bed level surface ($-\blacktriangle-$)

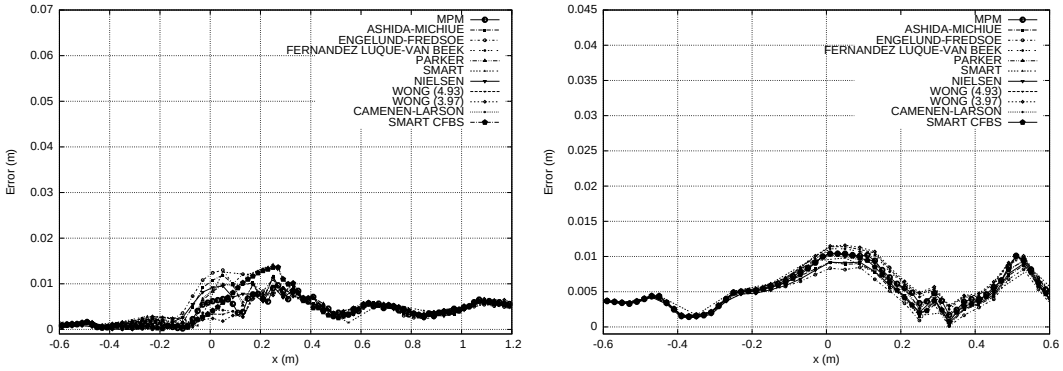

Figure 5.3: Modulus of the water level surface error (left) and bed level error (right) in x for the different formulations at $t = 1.5$ s in test A.

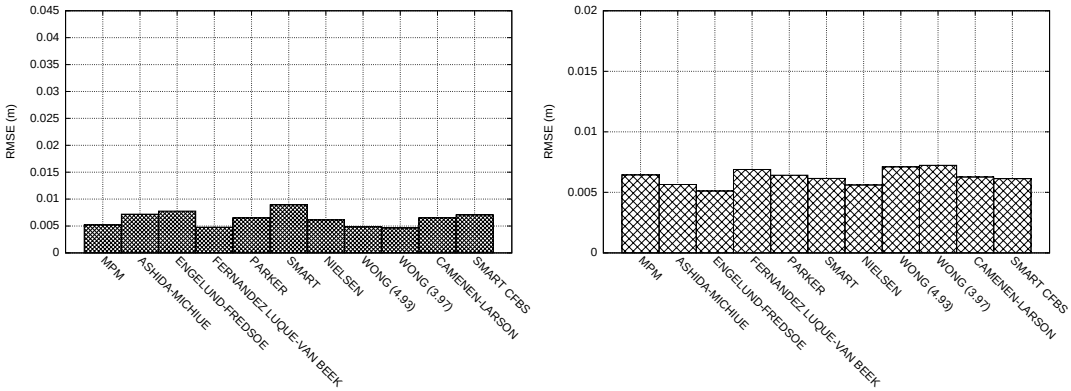

Figure 5.4: RMSE for water level surface (left) and bed level surface (right) with different formulas at $t = 1.5$ s in test A.

The similarity among computational results for the different discharge formulations is clear when observing Figure 5.3, that displays the modulus of the water level surface error (left) and bed level (right) error in x for the different formulations at $t = 1.5$ s. The RMSE (Root median square error) for the different formulations plotted at Figure 5.4, confirms that in plain bed, accurate results are given by all formulas.

5.2.2 Test B

Test B is a case of advance front over dry bed and adverse discontinuity. The flow developpes leading to a left moving rarefaction wave ending in front wave dominated by friction. Figure 5.5 shows again the numerical results and experimental data for the dam break test case B when using MPM (left) and Smart CFBS (right). In both cases, the most relevant difference with measured data is observed over the step, due to the lack of erosion with respect to experimental data. Upstream and downstream the step both numerical simulations provide identical results, being able to reproduce accurately the free surface level in space. Figure 5.6 shows how front wave celerity is well reproduced in time.

The lack of precision over the upward step is observed for all discharge formulations if observing Figure 5.7, that provides level errors in space. The rest of the domain

presents an acceptable error. The RMSE for water level surface (left) and bed level surface (right) at $t = 1.5$ s plotted at Figure 5.8 shows that in this test case there is not clearly a more advantageous formula.

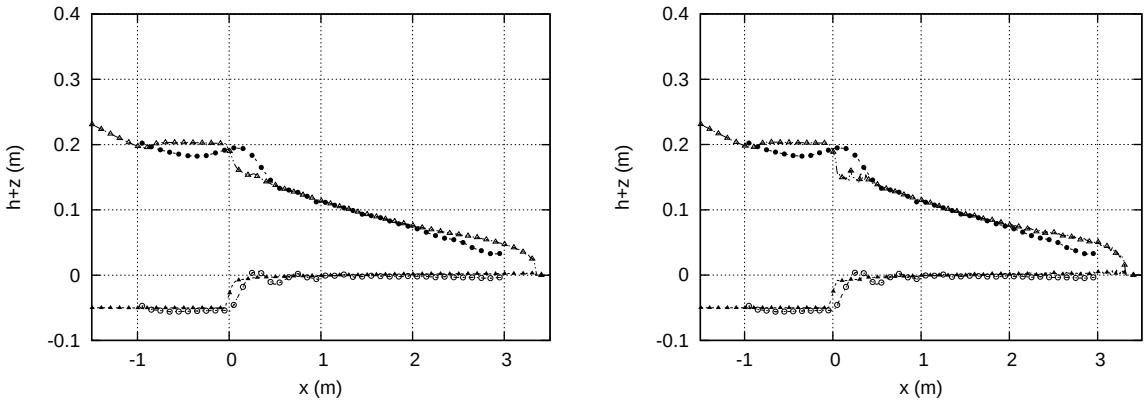

Figure 5.5: Numerical results and experimental data for the dam break test case B at $t = 1.5$ s, using a variable value of A_g computed using MPM (left) and Smart CFBS (right): measured water level surface ($-\bullet-$), measured bed level surface ($-\circ-$), computed water level surface ($-\triangle-$), computed bed level surface ($-\blacktriangle-$)

5.2.3 Test D

Test D represents a reservoir partially filled with sediments and includes a downward step. In this case, once flow passes through the gate location accelerates and decelerates in the friction dominated front. Figure 5.9 shows numerical results and experimental data for the dam break using MPM (left) and Smart CFBS (right). Smart CFBS formulation is able to handle perfectly with this kind of bed discontinuity, tracking the water level surface and redrawing correctly the bed level. Different time instants captured in Figure 5.10 allow appreciating the accuracy and the grade of detail of the computational results in time. Free surface and bed levels are correctly captured for both rarefaction wave and advance front wave, as well as, the bed level at the discontinuity point.

Figure 5.11 shows how Smart CFBS formulation provides the lowest level for bed level (right) and free surface (left) error in space at $t = 1.5$ s if compared with the rest of formulations. Also, the RMSE for water level surface (left) and bed level surface (right) displayed in Figure 5.12 confirms that Smart CFBS formulation gives the better results. Compared with test cases A and B, error is drastically reduced with the proposed formulation.

5.2.4 Test F

Test F is the last dam break studied in this paper. It is the case of a downward bed step combined with an initial layer of clear water in the downstream reach. The flows evolves in time leading to a left moving rarefaction wave upstream the gate, followed by an steady hydraulic jump downstream the gate and ending up in a right moving shock.

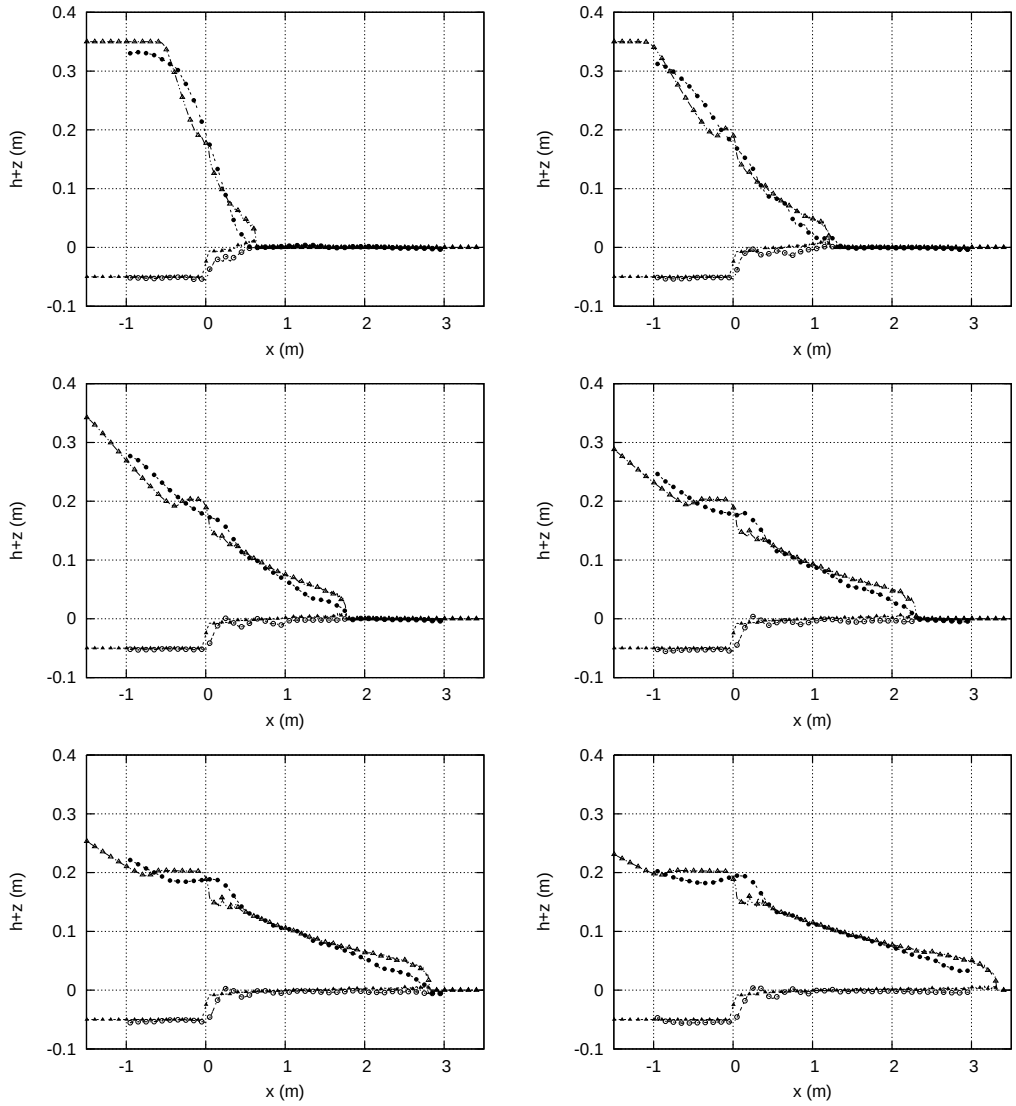

Figure 5.6: Numerical results and experimental data for the dam break test case B at times $t = 0.025$, 0.050, 0.075, 0.100, 0.125 and 1.5 s, using a variable value of A_g computed using Smart CFBS: measured water level surface ($-\bullet-$), measured bed level surface ($-\circ-$), computed water level surface ($-\triangle-$), computed bed level surface ($-\blacktriangle-$)

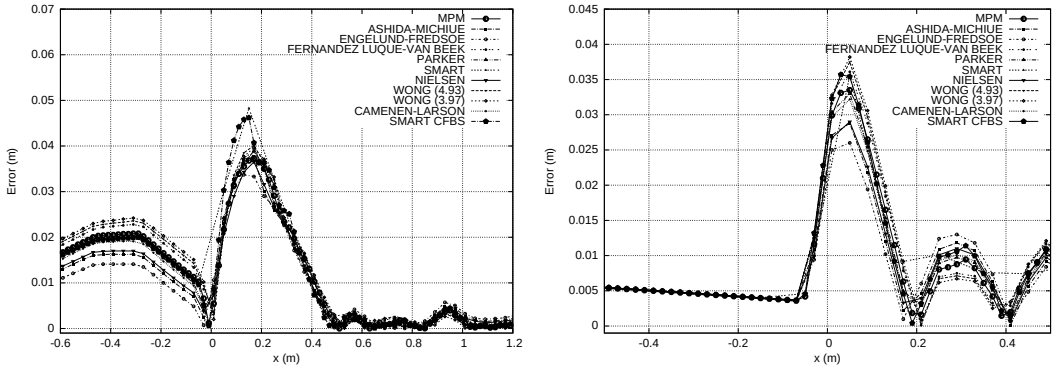

Figure 5.7: Modulus of the water level surface error (left) and bed level error (right) in x for the different formulations at $t = 1.5$ s in test B.

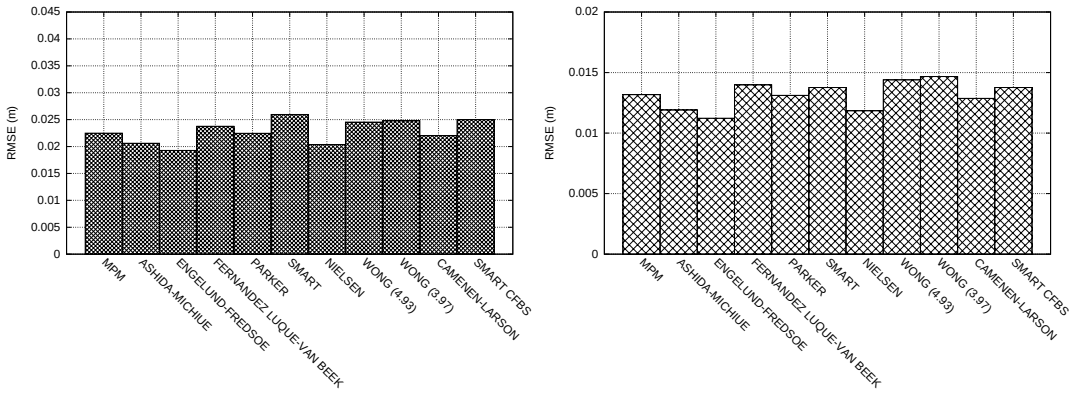

Figure 5.8: RMSE for water level surface (left) and bed level surface (right) with different formulas at $t = 1.5$ s in test B.

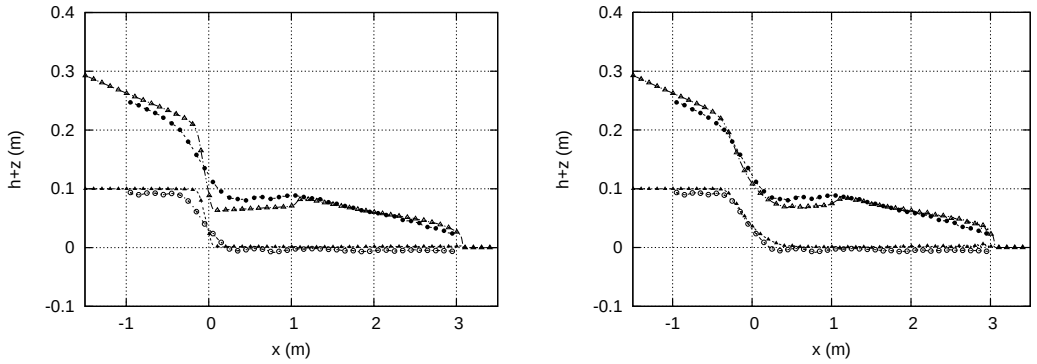

Figure 5.9: Numerical results and experimental data for the dam break test case D at $t = 1.5$ s, using a variable value of A_g computed using MPM (left) and Smart CFBS (right): measured water level surface ($-\bullet-$), measured bed level surface ($-\circ-$), computed water level surface ($-\triangle-$), computed bed level surface ($-\blacktriangle-$)

Figure 5.13 gathers numerical results and experimental data for the dam break test case F using MPM (left) and Smart CFBS (right). The results of Smart CFBS show that the experimental data is well depicted by numerical predictions in the rarefaction, the hydraulic jump and in the moving shock.

Figure 5.14 plots free surface and bed level at different times, where it can be observed how the shock celerity is perfectly captured by the numerical scheme in combination with Smart CFBS formulation. Small differences produced in the shock wave are attributable to fast transient energy variations associated to the existence of a hydraulic jump.

Smart CFBS leads to the smallest error in comparison with the other discharge formulas, as it is appreciated in Figure 5.15, where modulus of the water level surface error (left) and bed level error (right) in x are plotted. Figure 5.16 displays RMSE for water level surface (left) and bed level surface (right) with different formulas at $t = 1.5$ s leading to the same conclusion.

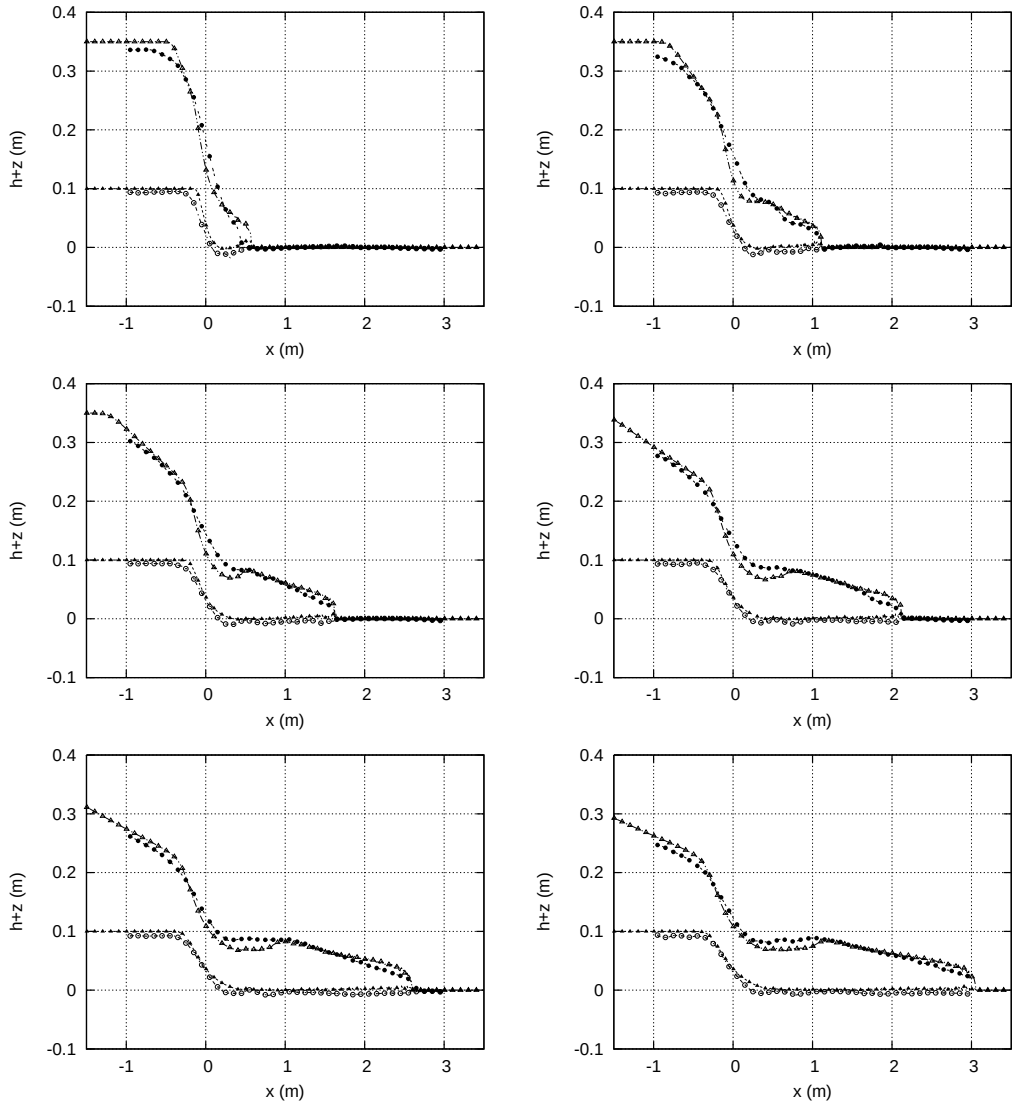

Figure 5.10: Numerical results and experimental data for the dam break test case D at times $t = 0.025$, 0.050, 0.075, 0.100, 0.125 and 1.5 s, using a variable value of A_g computed using Smart CFBS: measured water level surface ($-\bullet-$), measured bed level surface ($-\circ-$), computed water level surface ($-\triangle-$), computed bed level surface ($-\blacktriangle-$)

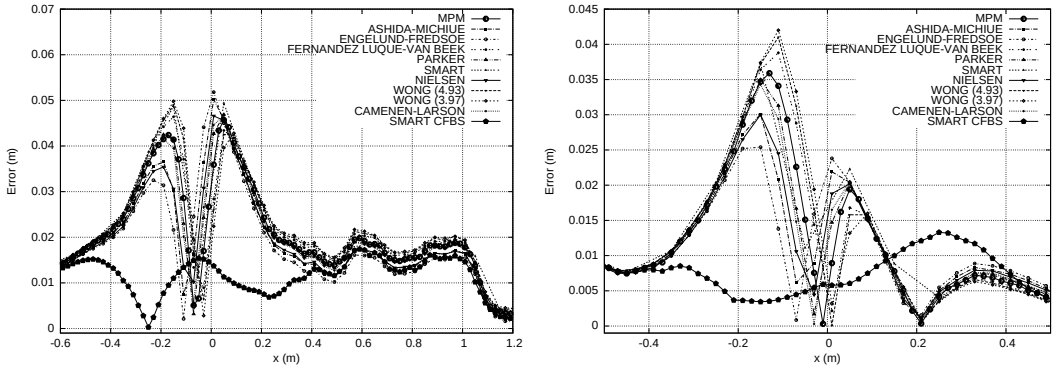

Figure 5.11: Modulus of the water level surface error (left) and bed level error (right) in x for the different formulations at $t = 1.5$ s in test D.

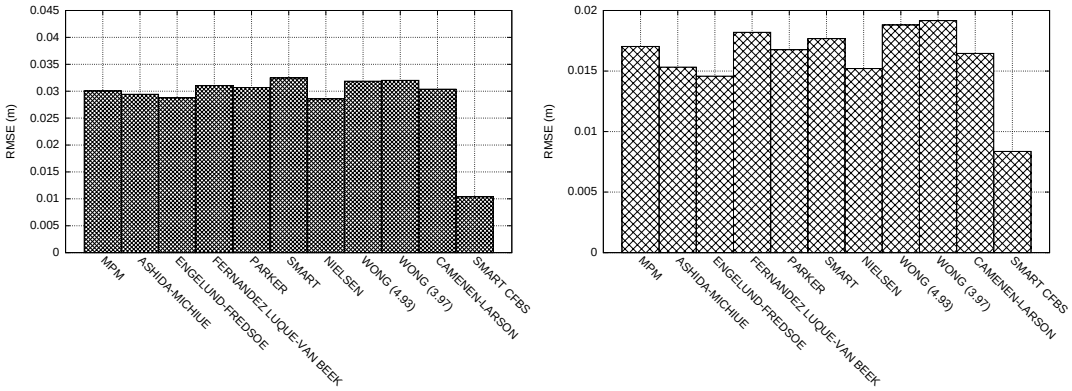

Figure 5.12: RMSE for water level surface (left) and bed level surface (right) with different formulas at $t = 1.5$ s in test D.

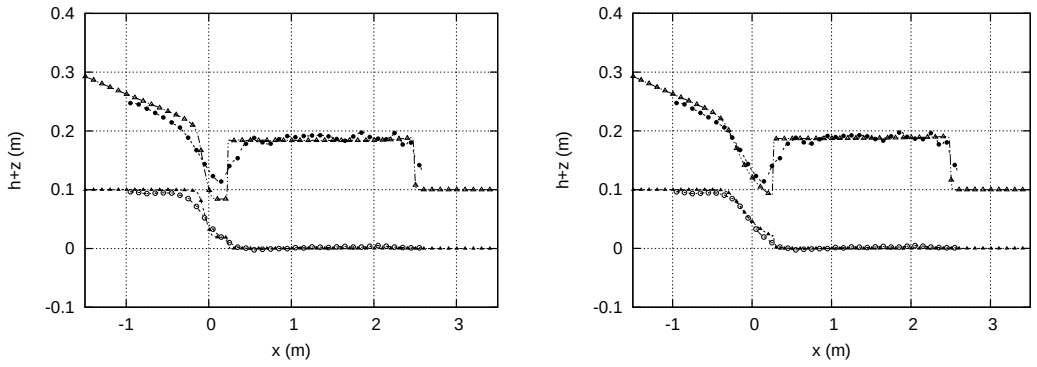

Figure 5.13: Numerical results and experimental data for the dam break test case F at $t = 1.5$ s, using a variable value of A_g computed using MPM (left) and Smart CFBS (right): measured water level surface ($-\bullet-$), measured bed level surface ($-\circ-$), computed water level surface ($-\triangle-$), computed bed level surface ($-\blacktriangle-$)

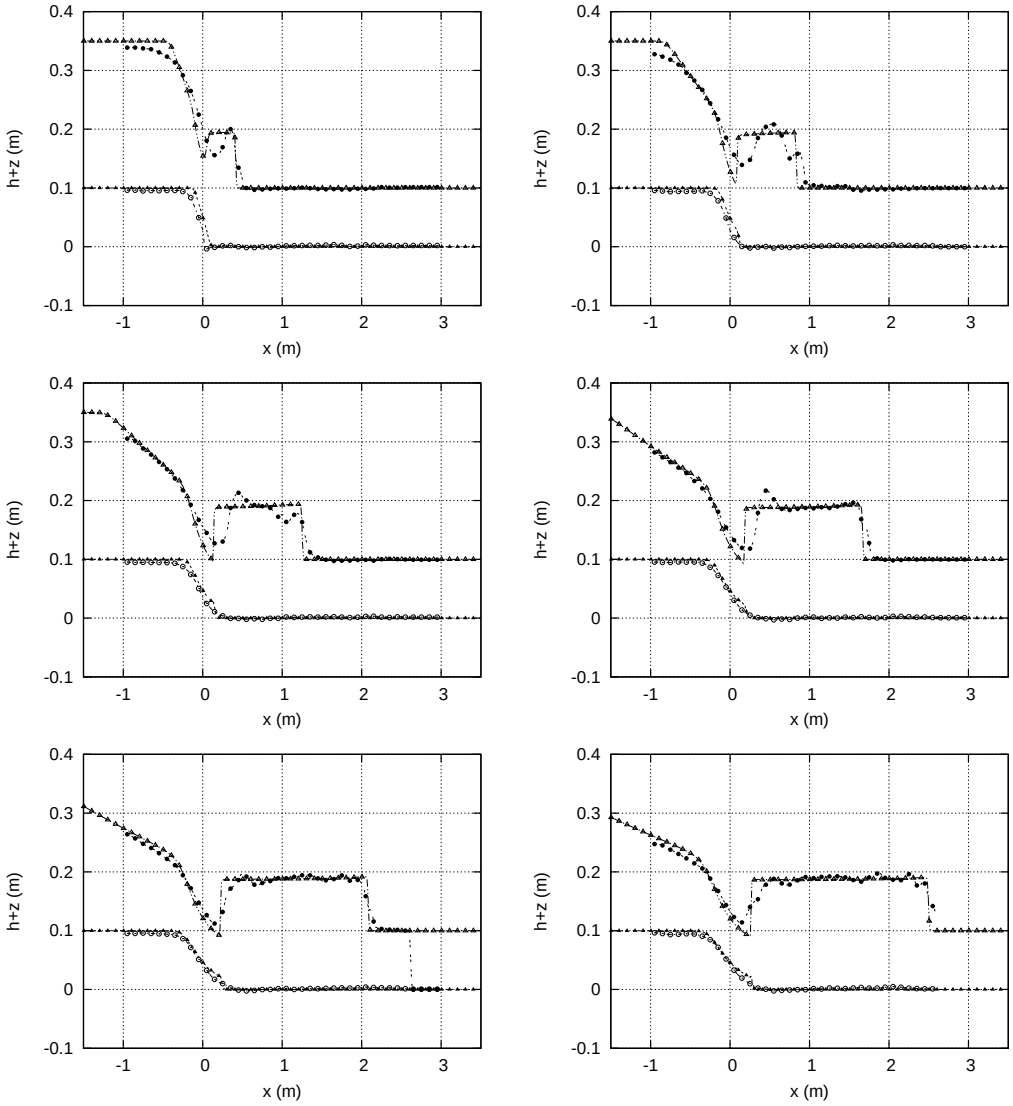

Figure 5.14: Numerical results and experimental data for the dam break test case F at times $t = 0.025$, 0.050, 0.075, 0.100, 0.125 and 1.5 s, using a variable value of A_g computed using Smart CFBS: measured water level surface ($-\bullet-$), measured bed level surface ($-\circ-$), computed water level surface ($-\triangle-$), computed bed level surface ($-\blacktriangle-$)

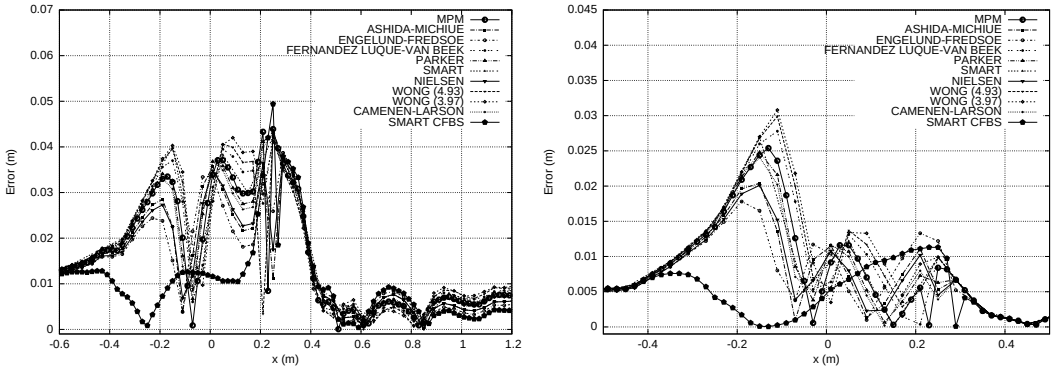

Figure 5.15: Modulus of the water level surface error (left) and bed level error (right) in x for the different formulations at $t = 1.5$ s in test F.

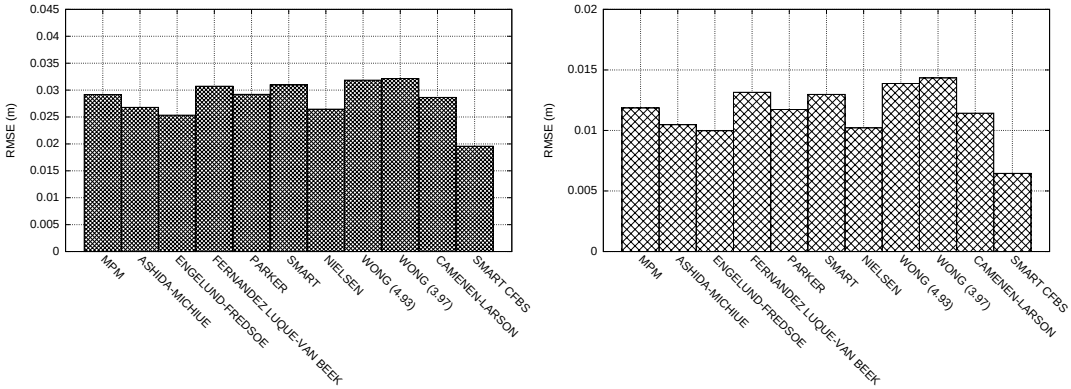

Figure 5.16: RMSE for water level surface (left) and bed level surface (right) with different formulas at $t = 1.5$ s in test F.

5.3 Numerical modelling of dam failure

Dam surface erosion and slope sliding failure in time due to flow overtopping was studied in Tingsanchali & Chinnarasri (2001). Figure (5.17) shows a sketch of the experimental setup. Experiments were carried out in a rectangular flume 35 m long, 1.0 m deep, and 1.0 m wide. The height and crest width of the dam were fixed at 0.80 m and 0.30 m. The upstream slope was fixed at 1V:3H, while the downstream slopes set to 1:5. The dam was made of sand with the following characteristics: $\rho_p = 2650 kgm^{-3}$, $d_{30} = 0.52mm$, $d_{50} = 0.86mm$, $d_{90} = 3.80mm$ and $d_m = 1.13mm$. A friction angle of $\varphi = 30^o$ was suggested, and the porosity was estimated using the formula Wu & Wang (2007):

$$p = 0.013 + \frac{0.21}{(d_{50}1000 + 0.002)^{0.21}} \tag{5.1}$$

and the Manning roughness coefficient by the Strickler formula:

$$n = \frac{1}{26} d_{90}^{1/6} \tag{5.2}$$

To have a uniform overflowing across the flume width, in the experiment reproduced

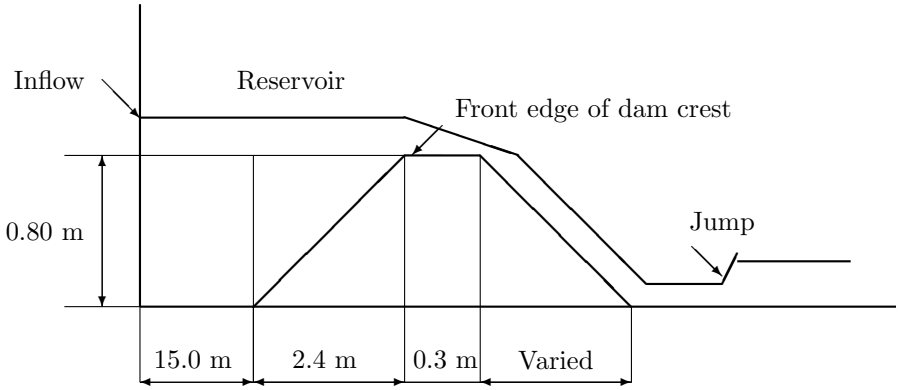

Figure 5.17: Sketch of the dam failure experimental setup.

in this work a vertical plate was held at the dam crest across the flume width until the upstream water level was 3 cm higher than the dam crest. The vertical plate was lifted up suddenly to allow the overflow to start.

In the dam breaching experiment three zones can be distinguished. The first is a subcritical region in the reservoir area, characterized by a very low velocity. The second zone is a supercritical region of highly unsteady flow over a steep bed slope in the downhill slope of the dam, starting at the front edge of the dam crest. The third zone, downstream of the dam is characterized by the presence of a hydraulic jump. The dam erosion model was computed in all cases using cells $\Delta x = 0.05$ m and CFL $= 1$.

During the development of this experiment bed level was recorded in time at three stations: SA, SB and SC, located respectively 15, 65 and 115 cm downstream from the edge of the original dam crest. The overtopping discharge was also caught along time, as well as, the reservoir level, just upstream the breach. The results presented below compare these experimental data with the computed ones, in order to validate the accuracy of the numerical method.

In Figure 5.18 (a) and (b) the numerical results for water level and bed level using MPM and Smart CFBS, respectively, are plotted. Figure 5.18 (c) and (d) show measured and computed bed level surface in time evolution at stations SA, SB and SC using MPM and Smart CFBS respectively. While MPM clearly underestimates the erosion rate, Smart CFBS provides results in good agreement with experimental data. Experimental and computed values of reservoir free surface level are displayed in Figure 5.19 (a) and (b) using MPM and Smart CFBS respectively. Better accuracy is reached when using the new proposed formulation.

Figure 5.20 (a) and (b) depicts the evolution in time of overtopping discharge using MPM and Smart CFBS respectively. It is observed that the maximum experimental overtopping discharge is reached by Smart CFBS while MPM predictions are quite far away from experimental data. Figure 5.20 shows the maximum overtopping discharge which is achieved with different formulas. The continuous line at the top of the im-

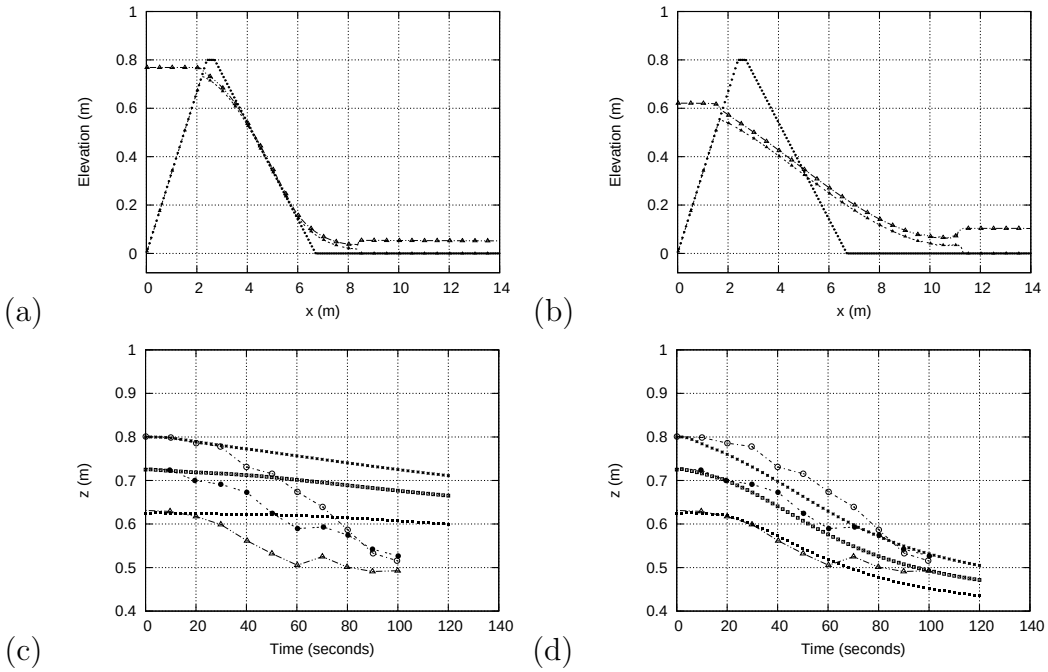

Figure 5.18: Results for Run case RB1. Initial bed level (- - -), computed water level surface ($-\triangle-$) and bed level surface ($-\blacktriangle-$) at $t = 120$ s using (a) MPM and (b) Smart CFBS. Bed level surface evolution in time measured at stations SA ($-\circ-$) ($-\square-$),SB ($-\bullet-$), and SC ($-\triangle-$) and computed at stations SA ($-\star-$),SB ($-\square-$), and SC ($-\blacksquare-$) using (c) MPM and (d) Smart CFBS.

age represents the maximum experimental overtopping discharge which is only well calculated with Smart CFBS formula.

Modulus of bed level error in time at stations SA, SB and SC with different formulas are shown in Figure 5.21 (a), (b) and (c), respectively. Smart CFBS formulation is the one which introduces less error in computed values. RMSE for bed level with different formulas in time appears plotted in Figure 5.21 (d). Newly, Smart CFBS presents the best agreement with experimental data in the three stations.

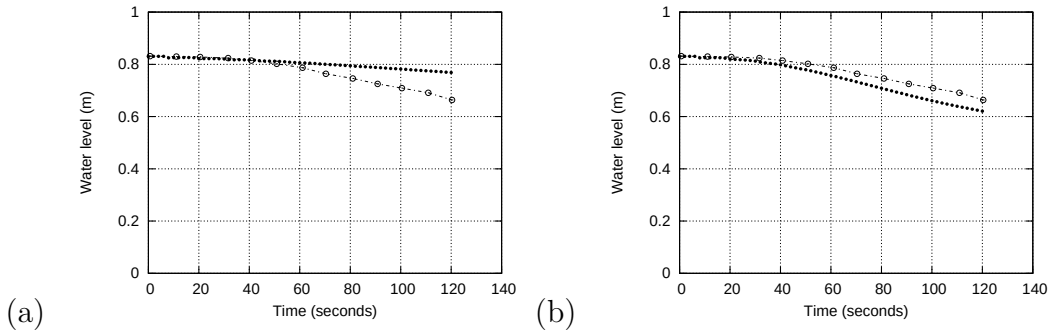

(a) (b)

Figure 5.19: Results for Run case RB1. Evolution in time of the measured water reservoir level ($-\circ-$) and computed water reservoir level ($-\bullet-$) using (e) MPM and (f) Smart CFBS.

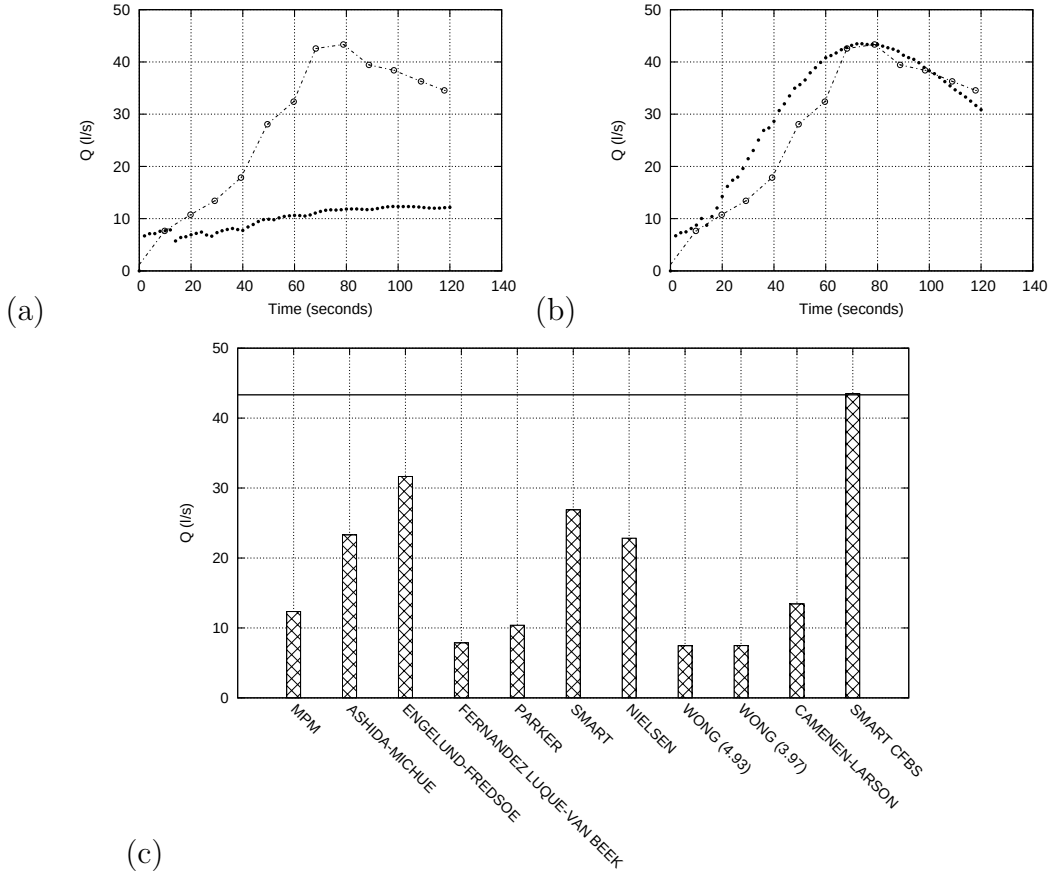

(a) (b)

(c)

Figure 5.20: Results for Run case RB1. Evolution in time of the measured ($-\circ-$) and computed ($-\bullet-$) overtopping discharge using (a) MPM and (b) Smart CFBS. Maximum overtopping discharge with different formulas (c).

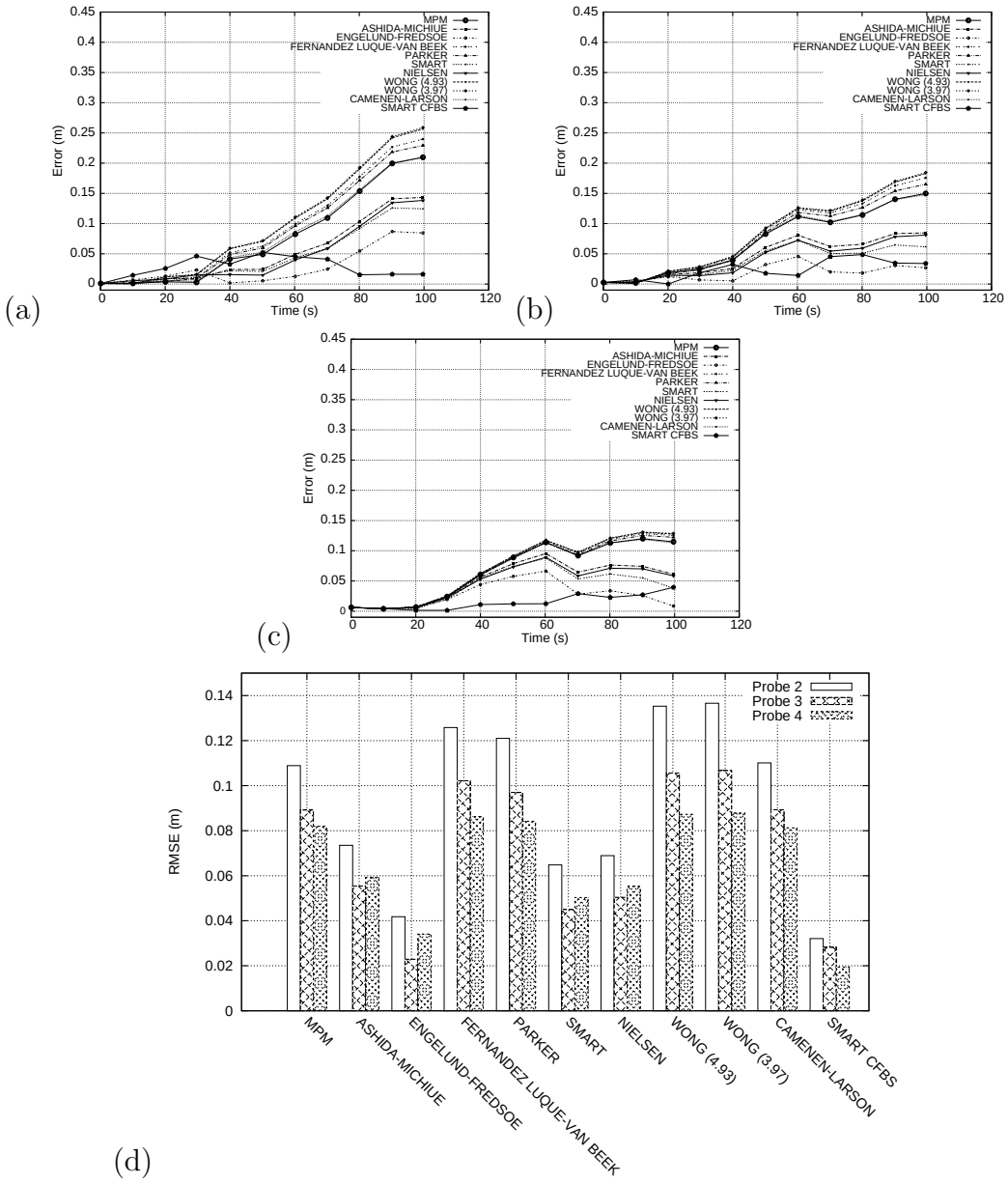

Figure 5.21: Results for Run case RB1. Modulus of bed level error in time at (a) station SA, (b) station SB and (c) station SC with different formulas. RMSE for bed level z with different formulas in time (d).

5.4 Sand cube

The last experiment studied in this paper is a test where the flow has a subcritical regime in opposition to previous tests. The experiment was made in a 15 m long channel, with a cross section of 0.5 x 0.5 m^2, at the Hydraulics Laboratory of the Civil Engineering School of the University of A Coruña (Spain) (Peña *et al.*, 2008).

The bottom of the flume was characterized by uniform slope, 0.00052, and a sediment layer 4.5 cm height, was placed in the central part, between 4.5 and 9 m from its upstream end. A sketch can be appreciated in Figure 5.22. The sand employed had the following properties: $\rho_s = 2680kgm^{-3}$, $d_{50} = 1mm$ (uniform size), $\varphi = 30^o$, negligible cohesion, porosity $p = 0.5$ and was characterized by a Manning roughness factor $n = 0.015$ sm$^{-1/3}$.

Initial conditions used were a water surface level downstream set to 0.115 m and a flow value enforced to be 21.8 l/s. Numerical simulations were performed using cells $\Delta x = 0.05$ m and CFL = 1.

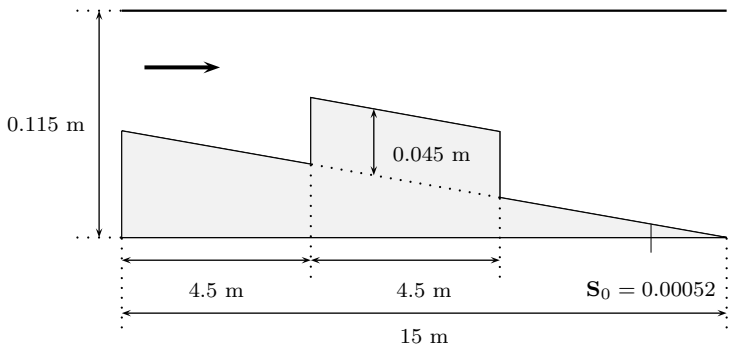

Figure 5.22: Sand cube sketch.

Figure 5.23 shows experimental data and numerical results calculated using MPM (left) and Smart CFBS (right) at different times. The bed evolution in time is well described with Smart CFBS. In the first part of the simulation there is an important mobilization of material up to time $t = 40$ min, when the sediment bed tends to stabilize. Most relevant differences between numerical and experimental data appear downstream the cube. This difference is more noticeable at time $t = 120$ min and is attributable to the fact that in the sediment transport model suspended load is not considered. A careful data analysis of the measured bed level reveals that at this time, the initial mass associated to the cube is not conserved, may be due to suspension effects. On the other hand, the numerical scheme used in this work is exactly mass conservative, so differences between numerical and experimental data downstream the cube are expectable. The results provided by MPM formula are unable to gather information correctly, leading to a poor bed level prediction as time increases.

Correct performance of Smart CFBS in comparison with the rest of sediment discharge formulae is well appreciated in Figure 5.24, where the modulus of bed level error in x (left) and RMSE for bed level surface at time $t = 120$ min (right) are plotted. Smart CFBS presents the more accurate results.

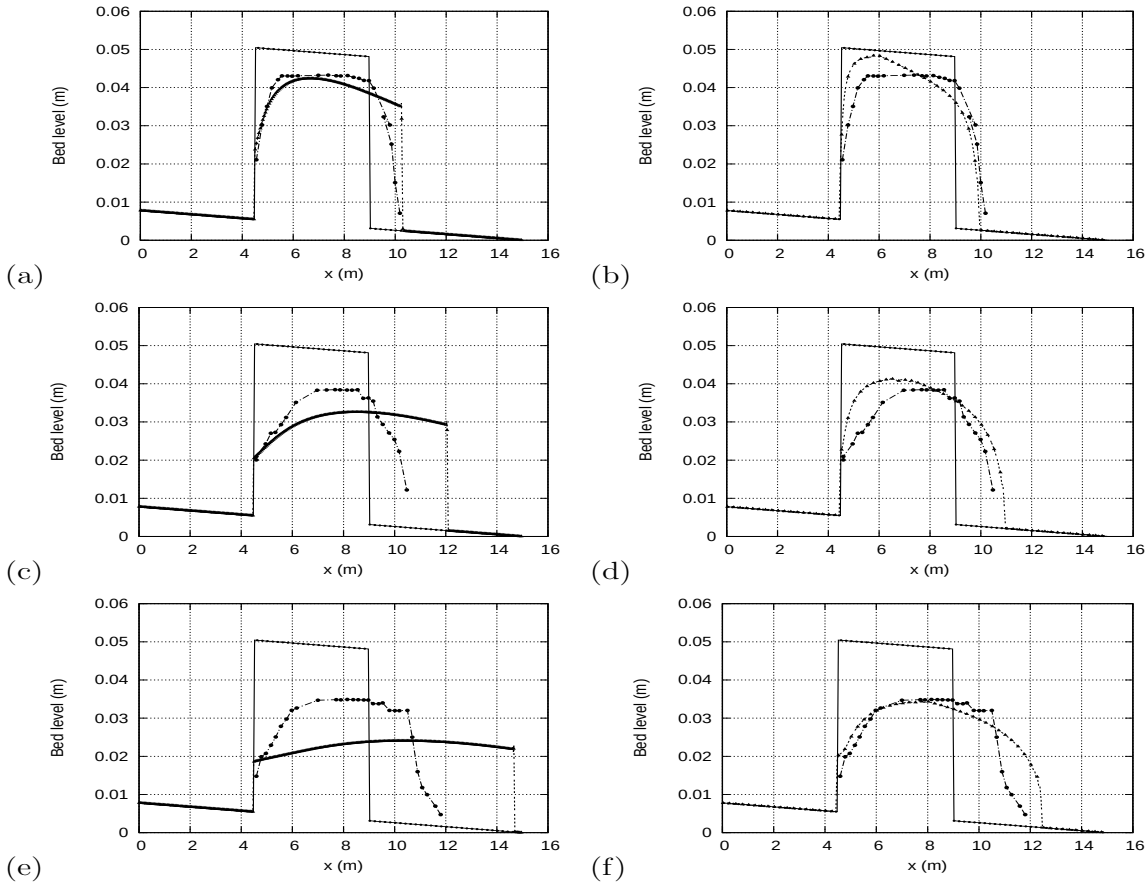

Figure 5.23: Results for the sand cube test case. Initial bed level ($\cdots$), measured bed and water level ($-\bullet-$) and computed ($-\triangle-$) using MPM at times (a) $t = 10$ min, (c) $t = 40$ min, (e) $t = 120$ min, and using Smart CFBS at times (b) $t = 10$ min,(d) $t = 40$ min, (f) $t = 120$ min.

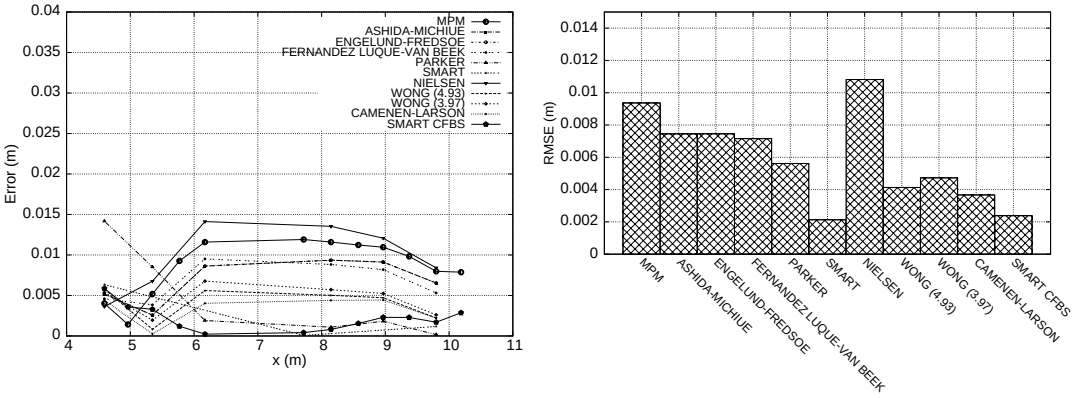

Figure 5.24: Results for the sand cube test case. Modulus of the bed level error in x for the different formulations after 120 min (left) and RMSE for bed level surface with different formulae at 120 min (right).

Chapter 6

Two dimensional cases

6.1 Introduction

Considering the increasing complexity in 2D flow with respect to 1D cases, and the fact that well proven capacity formulas are based on 1D experimental steady flows, the performance of different closure formulas in unsteady 2D numerical models must be carefully analyzed. In order to ensure the reliability of the numerical experimentation, the formulation has to be general enough in order to allow for the use of different empirical laws and the numerical scheme must handle correctly the coupling between the 2D shallow-water equations and the Exner equation under any condition. In this chapter the relative performance of the sediment formulae presented in chapter 3, for the cases of a dam failure and a dam break in a channel with a symmetric enlargement, are compared in bidimensional unsteady situations.

6.2 Numerical modelling of dam failure

Dam surface erosion and slope sliding failure modeling in time due to flow overtopping was studied by Tingsanchali et al. in Tingsanchali & Chinnarasri (2001). A sketch of the experimental setup and laboratory conditions are detailed in previous chapter, Figure 5.17. Being the flow mostly onedimensional in this case, it is important to check the performance of the numerical discretization of the empirical formulations in a 2D mesh to ensure that numerical results are not influenced by the grid definition. This case is of great interest, as it allows a direct comparison between 1D and 2D simulations in a wide variety of flow conditions.

2D numerical simulations have been performed using a coarse unstructured triangular mesh, with a maximum cell size of 0.01m^2, Figure 6.1. The CFL is retained equal to 0.5 in all the simulations, and the bed has been considered deformable in all the domain. No boundary condition has been imposed at the outflow section. Figure 6.2 displays the numerical results obtained using Smart CFBS formulation for both the water level and the bed level. During the first seconds the erosion rate reduces drastically the height of the crest and downstream the dam a hydraulic jump appears. At the final stage

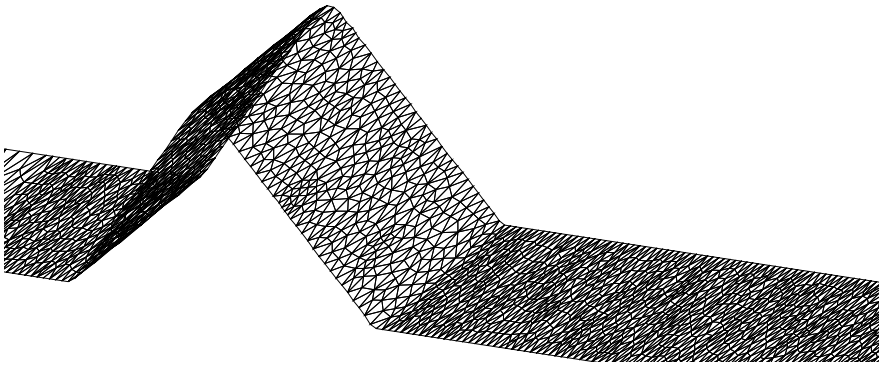

Figure 6.1: Detail of the triangular mesh

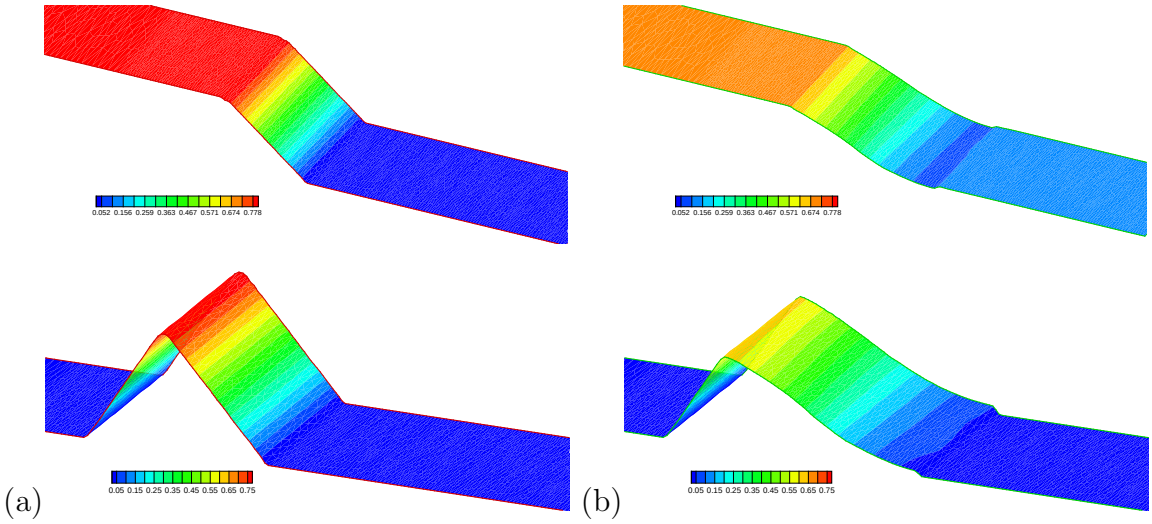

(a) (b)

Figure 6.2: Numerical results of water level (top image) and bed level (bottom level) in the dike at 0s (a) and 120s (b) using Smart CFBS formulation.

of the simulation, a large wedge has been developed. Also, the presence of incipient antidunes is observed.

Figures 6.3 (a) and (b) show the water and bed level surface computed after 120s using MPM and Smart CFBS formulations respectively. The bed level evolution recorded in time at the three stations SA, SB and SC, located downstream from the edge of the original dam crest, are plotted in Figures 6.3 (c) and (d). The evolution of the measured and computed water reservoir level is depicted in Figures 6.3 (e) and (f). In all cases the Smart CFBS formulation presents accurate results, while the MPM formulation shows noticeable discrepancies with respect to the experimental data.

Figures 6.4 (a) and (b) display the measured and computed overtopping discharge just upstream the breach using MPM and Smart CFBS formulations respectively. It is observed that the experimental overtopping discharge is better tracked with Smart CFBS while MPM predictions are quite far from experimental data.

The relative performance of the different formulations in terms of RMSE is plotted in Figure 6.5 at the three stations SA, SB and SC, showing important differences among numerical results depending of the experimental law selected. The Engelund and Fredsoe sediment transport relation was derived for a wide range of slopes, and Figure 6.5

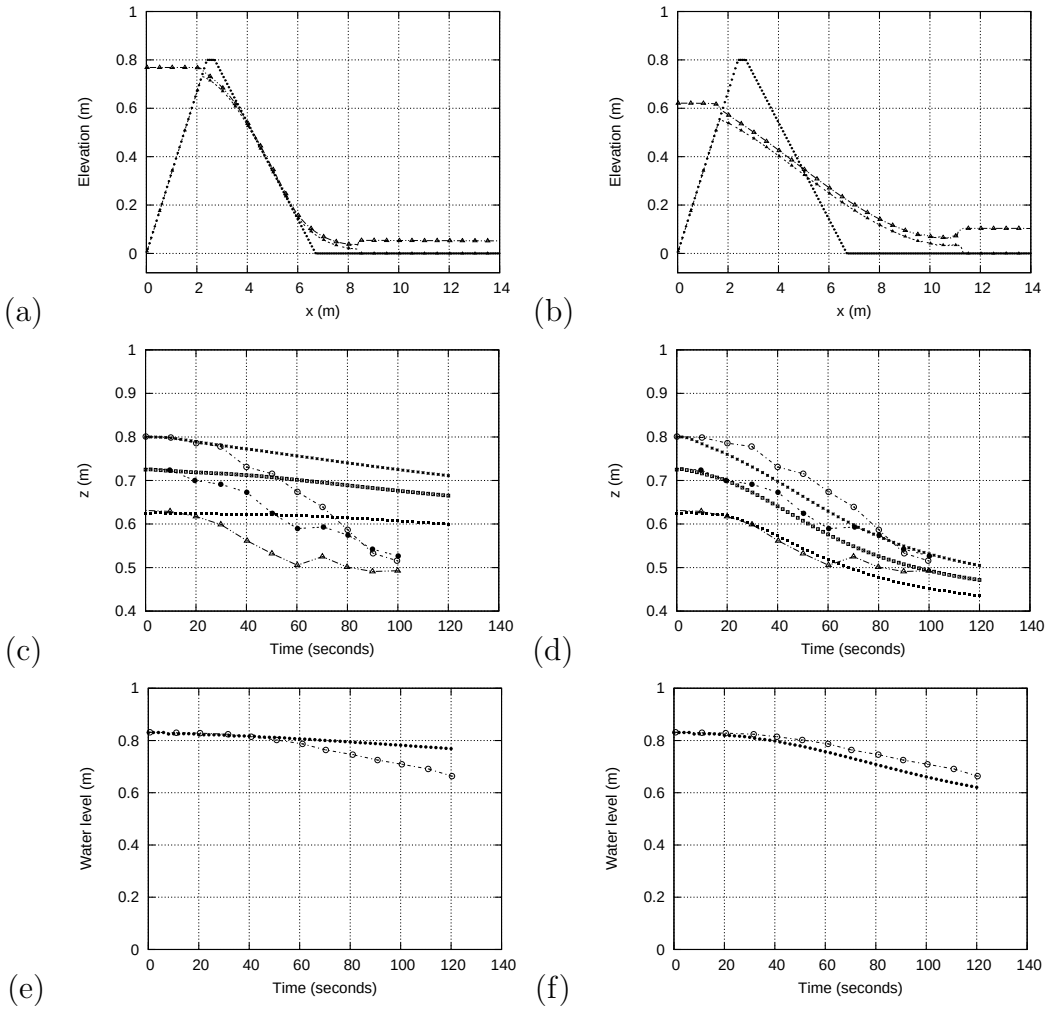

Figure 6.3: Initial bed level (- - -), computed water level surface ($-\triangle-$) and bed level surface ($-\blacktriangle-$) at $t = 120$ s using (a) MPM and (b) Smart CFBS. Bed level surface evolution in time measured at stations SA ($-\circ-$) ($-\square-$),SB ($-\bullet-$), and SC ($-\triangle-$) and computed at stations SA ($-\star-$),SB ($-\square-$), and SC ($-\blacksquare-$) using (c) MPM and (d) Smart CFBS. Evolution in time of the measured water reservoir level ($-\circ-$) and computed water reservoir level ($-\bullet-$) using (e) MPM and (f) Smart CFBS.

shows how this formulation leads to low values of RMSE. The Smart formula was derived for a set of experimental cases with steep slopes, therefore it can be expected that in this case any numerical discretization would provide accurate predictions. Contrarily, numerical simulation shows that the Smart FS discretization leads to less accurate results if compared with those given by the Smart CFBS discretization. The rest of formulations, derived from experiments ranging from low to medium slopes provide higher RMSE.

When comparing the numerical results of the 2D simulation with those obtained of a 1D discretization, it can be observed that the RMSE is slightly bigger in the 2D cases and that 2D results follow closely the tendencies given by the 1D formulation.

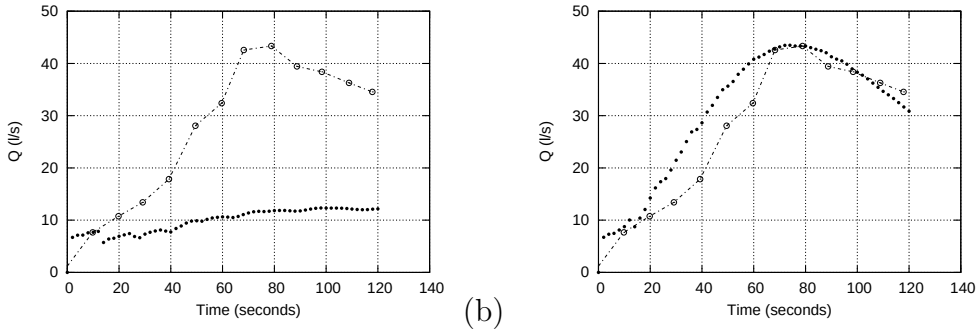

(a) (b)

Figure 6.4: Evolution in time of the measured ($-\circ-$) and computed ($-\bullet-$) overtopping discharge using (a) MPM and (b) Smart CFBS.

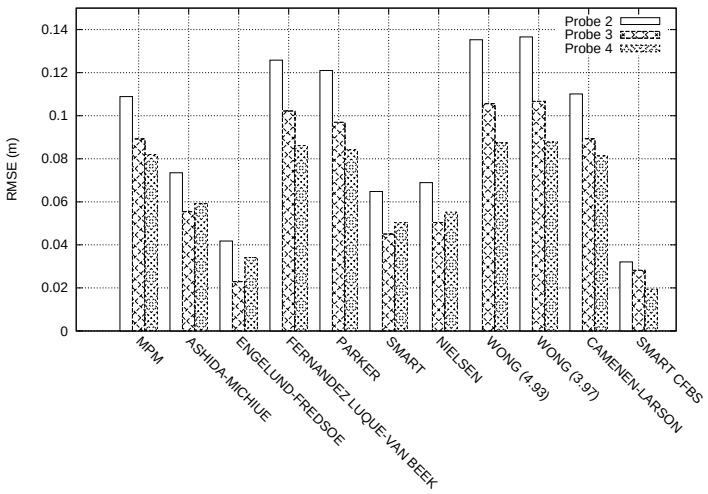

Figure 6.5: RMSE for bed level z at stations SA, SB and SC ($-\triangle-$) with different formulas in time.

6.3 Symmetric configuration for dam break flow over erodible bed

This experiment was designed at the laboratory of UCL (Soares *et al.*, –) consisting of a dam break over a 3.6 m wide and about 36 m long flume. The gate was connected to an upstream reservoir and was 1 m wide. The sand was extended over 9 m downstream the gate and 1 m upstream the gate, having a thickness of 0.085 m. A complete sketch of the set up of the experiment is shown in Figure 6.6. The properties of the sand were $\rho_s = 2630$ kg m^{-3}, $d_{50} = 1.61$ mm, $\varphi = 30^o$, negligible cohesion, porosity $p = 0.40$ and was characterized by a Manning roughness factor n= 0.019 sm$^{-1/3}$. Initial conditions used were: upstream, the water level was imposed to 0.047 m, and downstream, a control section at the end of the flume with the same height as the sand layer, 0.085 m. The measurements carried out during the experiments consisted of recording the water level evolution for the first 20 s at different probes, Figure 6.7, and the longitudinal bed profiles measured from $x = 0.5$ m to $x = 8$ m at two y coordinates, Table 6.1, and at $t = 100$ s.

The domain was discretized on a non-uniform triangular mesh, with a higher density downstream the widening, being the total number of cells equal to 12500. The CFL used was imposed to 0.5.

Table 6.1: Position of the sections

Section	*Y coordinate (m)*
S1	0.20
S2	0.70

Figures in 6.8 show a sequence of plant views of the computed bed evolution in time predicted by the Smart CFBS discretization, characterized by fast morphodynamic changes. Figure 6.8 (a) at $t = 10$ s shows how the flow generates a wavefront which causes an important erosion process in the enlargement zone of the channel. While the flooding wave advances the sand particles grabbed in this process are carried out to the wavefront and to the wall, where they tend to sediment, as shown in Figure 6.8 (b) at $t = 20$s respectively. Symmetric elongated sedimentary bodies appear on the right and left banks of the channel, that grow in time to merge generating a diamond-shaped erosion region at $t = 40$s, shown in Figure 6.8 (c). At $t = 60$ s most of the morphodynamic changes have taken place, and the drainage of the water contained in the upstream reservoir smooths the bed surface, attenuating the bed forms previously generated. For longer times, no more important morphodynamic changes happen. At $t = 100$ s, Figure 6.8 (f) shows how only the diamond-shaped erosion region in the enlargement zone, generated by the sudden change in flow direction after the opening of the gate, remains in time. The rest of the bed surface becomes almost planar.

Figure 6.9 displays the final bed surface at $t = 100$ s obtained with the experimental data (left) and with the numerical results using Smart CFBS formula (right). Numerical results follow correctly the tendency of the final bed morphology although they tend to underestimate the length of the diamond-shaped body and the thickness of the

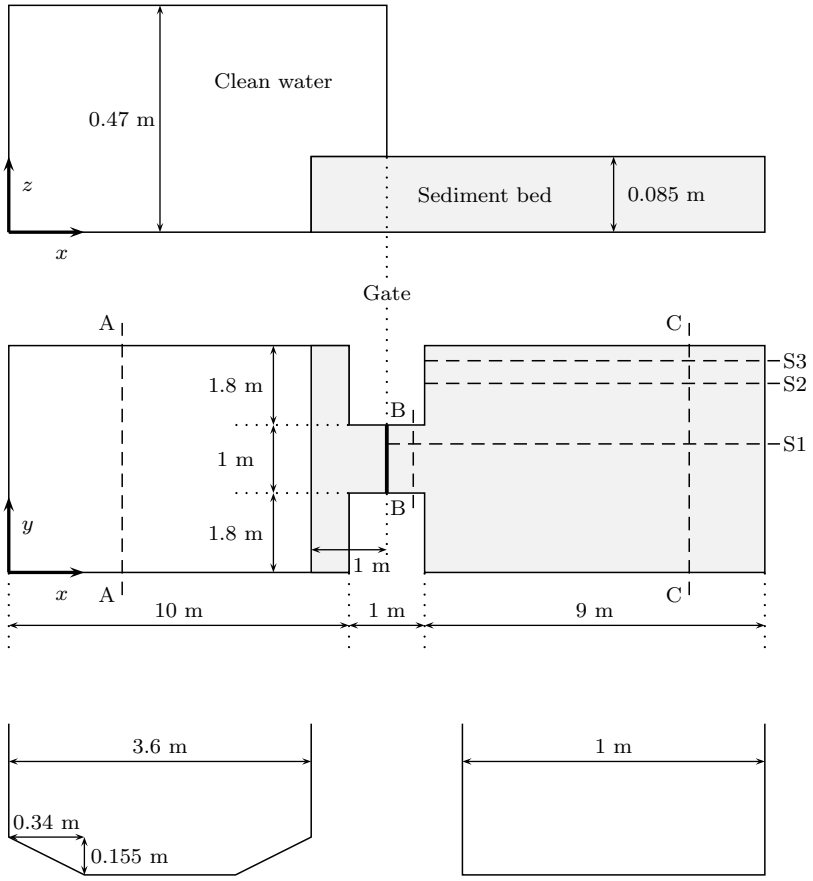

Figure 6.6: Experimental set up: transversal sketch, 2D sketch and cross secctions (AA-CC and BB).

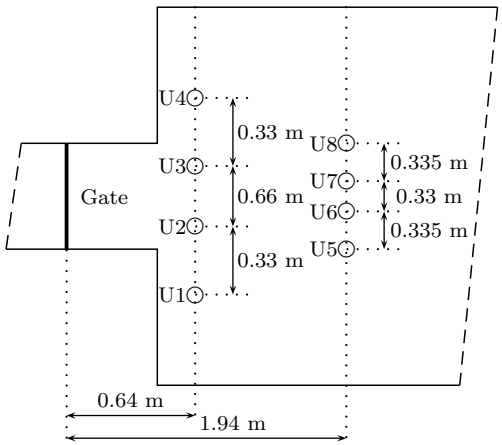

Figure 6.7: Position of probes in the experiment

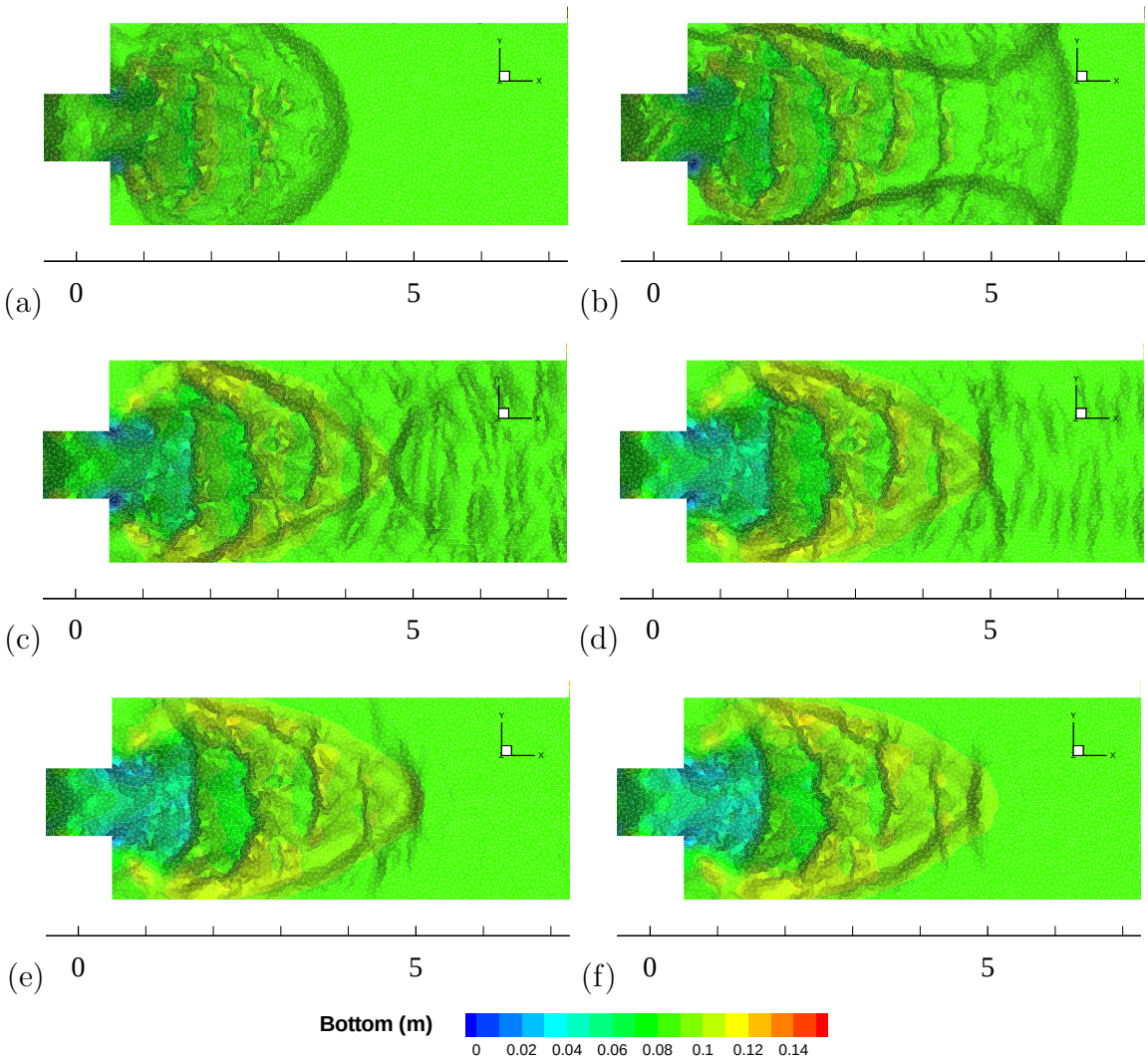

Figure 6.8: Numerical results of bed level in the enlargement zone at 10s (a), 20s (b), 40s (c), 60s (d), 80s (e) and 100s (f) using Smart CFBS formula

eroded layer, resulting in smaller heights for the deposition forms. In the experimental data the length of the bed-form zones is bigger than the one provided by the numerical simulation. This may be explained, if considering that, due to the underestimation of erosion rates along the numerical simulation, the magnitude of the bed forms is smaller, and consequently, they are more easily eroded. Also, differences between numerical and experimental bed surfaces can be justified by two important points: i) the 2D SW model neglects the vertical accelerations and decreases the erosion/deposition rate and ii) errors associated to the reconstruction of the experimental bed surface, which was generated through the interpolation of measured bed profiles.

The results shown in, Figures 6.10, 6.11, display the experimental bed level against the computed one using the MPM and the Smart CFBS formulae at the two control sections. The first one, section S1, which is placed to study the effect of the flow over the bottom in the enlargement zone presents differences between both load discharge formulae. The Smart CFBS formula obtains a better tracking of the sedimentary proccess, getting more accurate results for the maximum erosion position, $x = 1.4$ m,

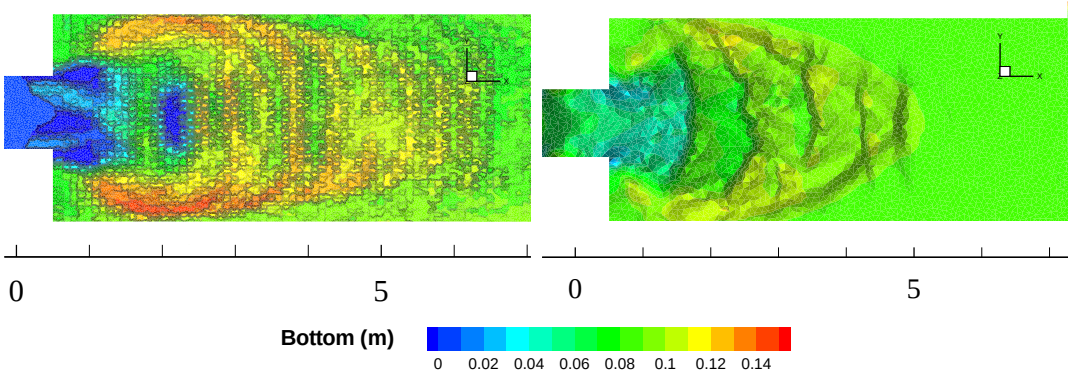

Figure 6.9: Experimental results (left) and numerical results using Smart CFBS formula (right) of bed level in the enlargement zone at 100s

and in the maximum deposition position, $x = 2.6$ m.

At the second control section, section S2, differences are also noticeable between both sediment transport formulae, being the Smart CFBS the formula which achieves a better averaged bed level. The computed results obtained with MPM show a zone at $x = 1.2$ m where erosion is clearly overestimated.

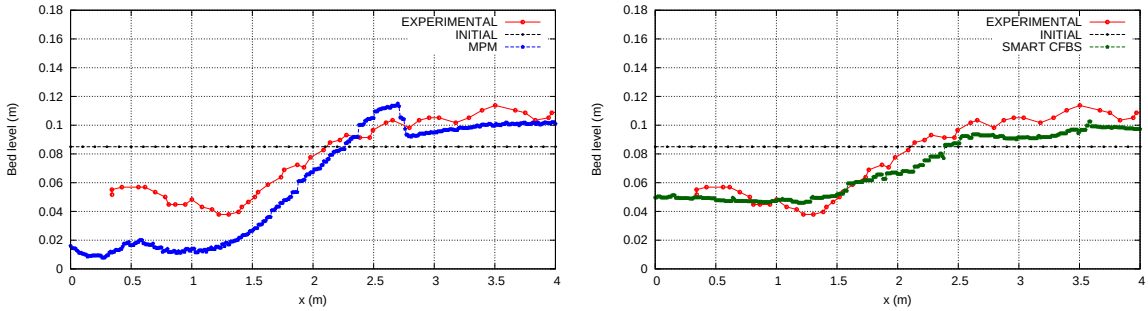

Figure 6.10: Numerical results of bed level with MPM (left) and Smart CFBS (right) against experimental data at section S1 ($y = 0.2$ m) and at $t = 100$ s

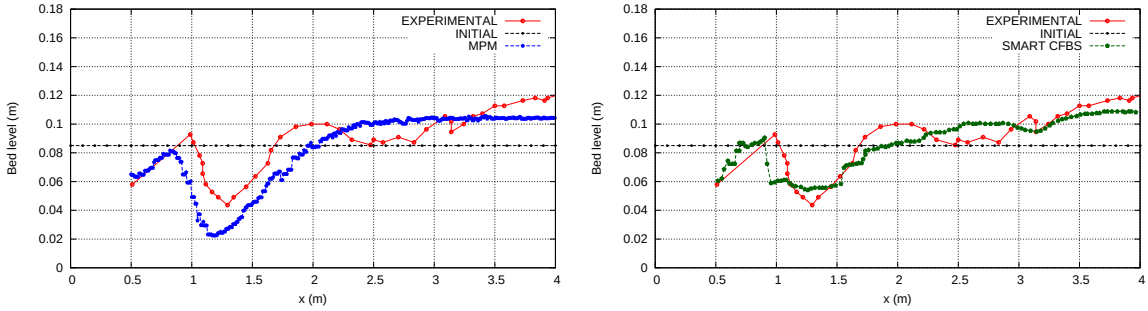

Figure 6.11: Numerical results of bed level with MPM (left) and Smart CFBS (right) against experimental data at section S2 ($y = 0.7$ m) and at $t = 100$ s

The RMSE of every section and every bed load discharge are shown in Figure 6.12. The results obtained with Smart CFBS are always among the ones which provide less error.

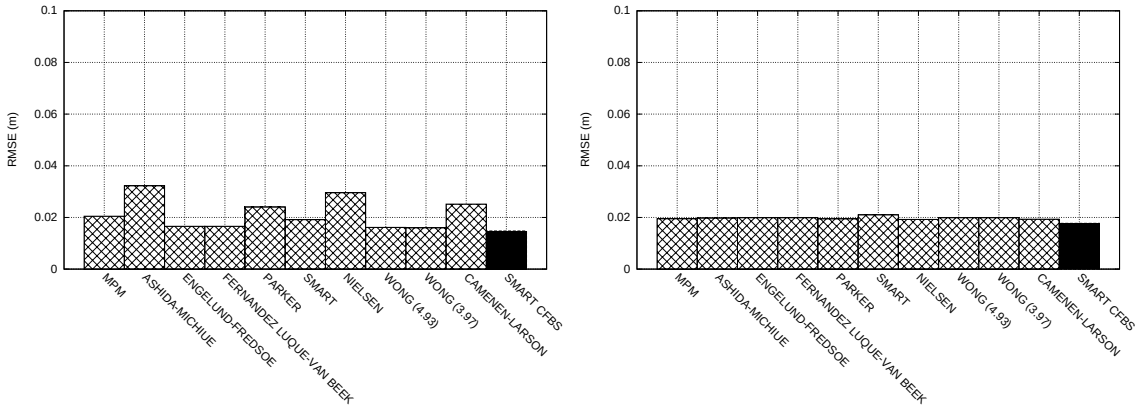

Figure 6.12: RMSE values corresponding to the two control sections, S1 (left) and S2 (right), and obtained with every sediment transport formula

In the case of the probes, the results are presented in Figures 6.13 and 6.14. The water level measured is compared with the results obtained using the MPM and Smart CFBS formulae. Both formulations provide similar values, except at probes U2 and U3 where the Smart CFBS formula shows a better tracking of the water level evolution in time. Probes which are further from the widening location obtain more accurate predictions and this is justified by the reduced influence of the erosion/deposition rates in those zones.

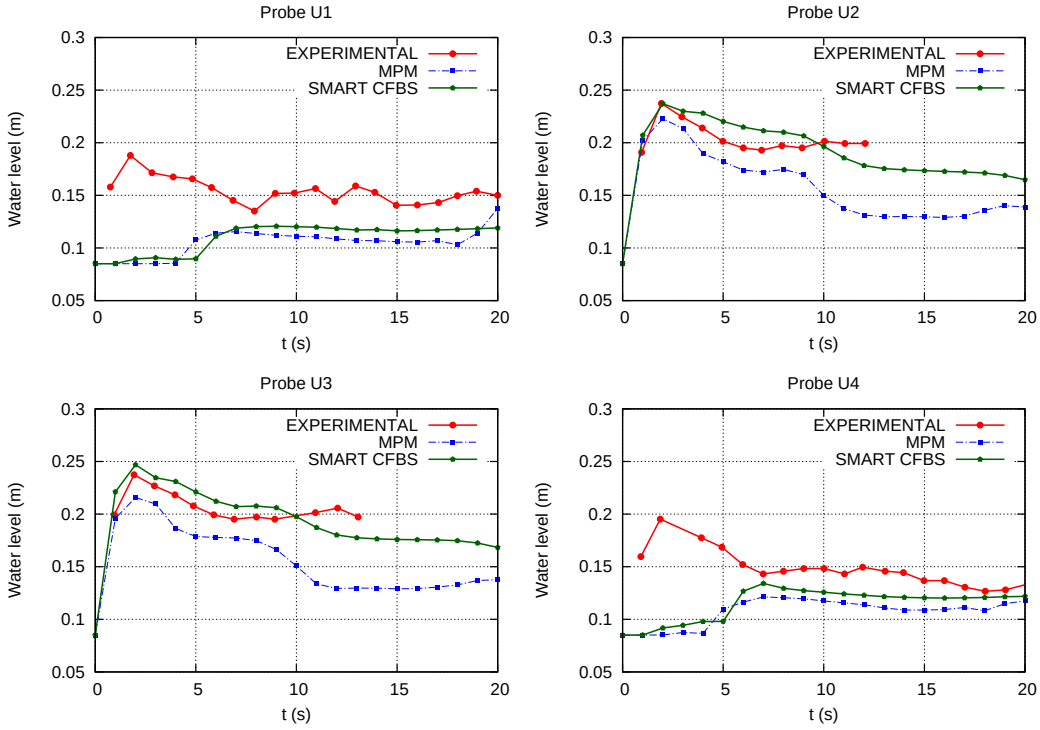

Figure 6.13: Probe U1 ($x = 0.64$ m, $y =$ -0.99 m). Probe U2 ($x = 0.64$ m, $y =$ -0.33 m). Probe U3 ($x = 0.64$ m, $y = 0.33$ m). Probe U4 ($x = 0.64$ m, $y = 0.99$ m). Comparison between experimental values and MPM and Smart CFBS water level at $t = 20$ s

The RMSE value associated to every probe and to every bed load transport formula is displayed in Figures 6.15 and 6.16. The RMSE provided by probes which are close

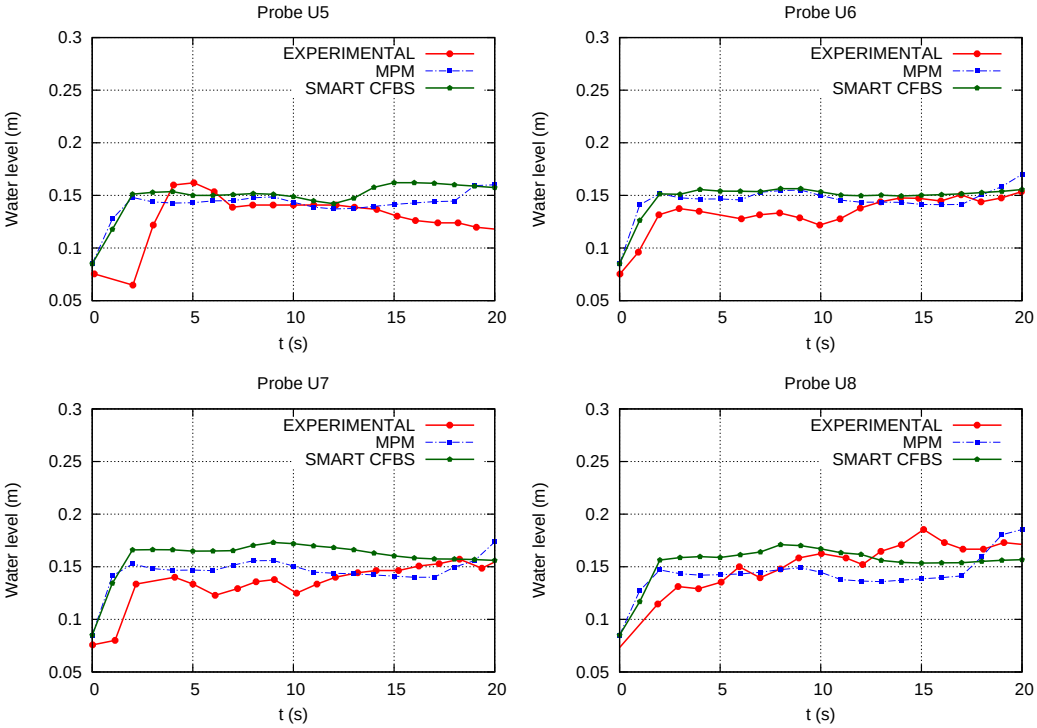

Figure 6.14: Probe U5 ($x = 1.94$ m, $y =$ -0.5 m). Probe U6 ($x = 1.94$ m, $y =$ -0.165 m). Probe U7 ($x = 1.94$ m, $y = 0.165$ m). Probe U8 ($x = 1.94$ m, $y = 0.5$ m). Comparison between experimental values and MPM and Smart CFBS water level at $t = 20$ s

to the enlargement zone, U1, U2, U3 and U4, presents a bigger error, as it is has been argued previously. Smart CFBS formula is always between formulations with less associated error.

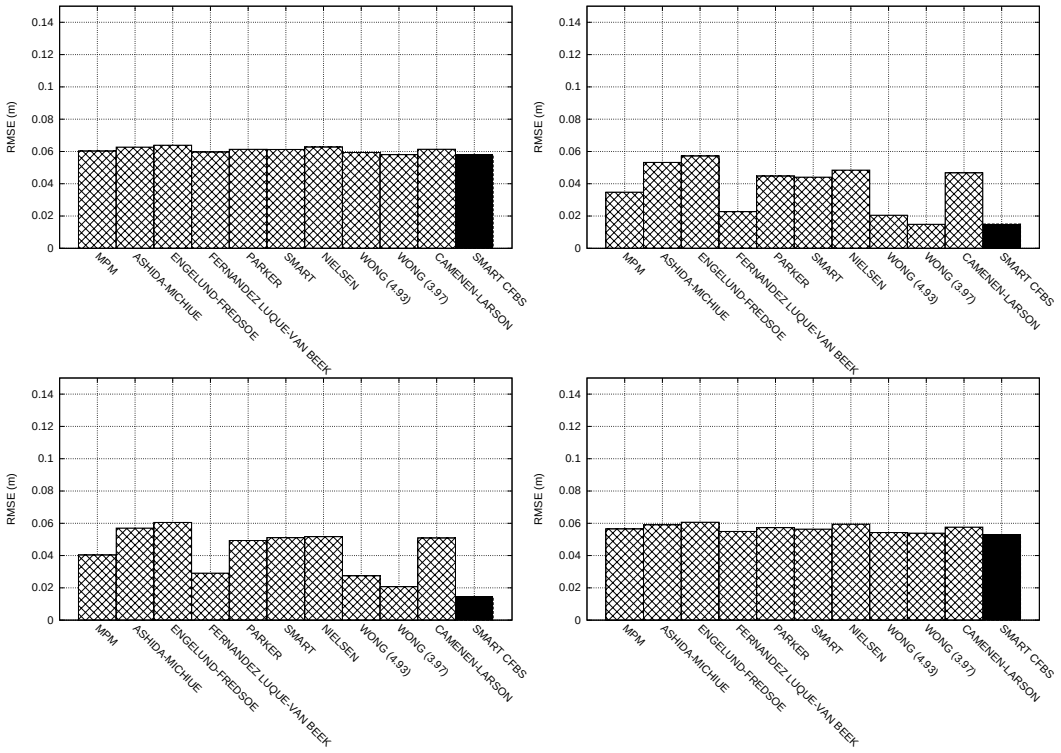

Figure 6.15: RMSE values corresponding to four probes (U1, U2, U3, U4, from left to right and from top to the bottom) and computed for every sediment transport formula

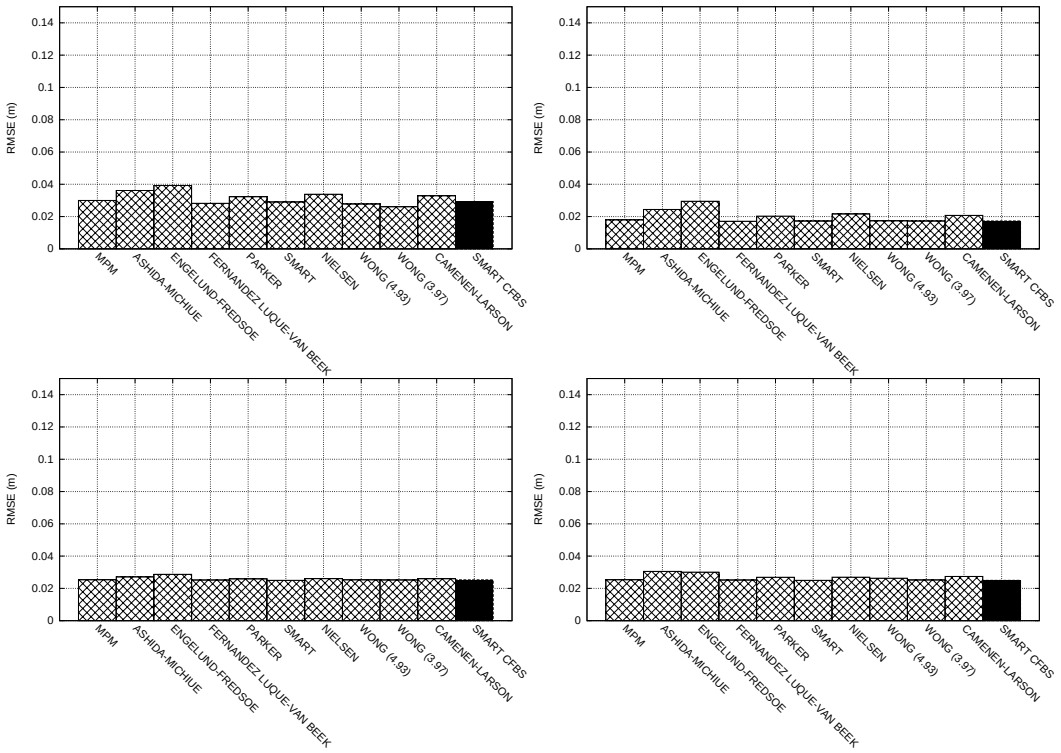

Figure 6.16: RMSE values corresponding to four probes (U5, U6, U7, U8, from left to right and from top to the bottom) and computed for every sediment transport formula

Chapter 7

Conclusions and further research

7.1 Conclusions

1D test cases

In the first set of test cases, the bed load formulae have been applied to solve dam break flows over dry/wet initial conditions. Whilst advance front celerity has been well captured in the dam break cases over dry bed with independence of the type of capacity formula used, noticeable differences appear in the bed level predictions, except in the dam break test case A with initially flat bed level and in the case B with adverse slope. In experiment D, over favorable slope and dry bed, erosion produces a meaningful variation of the initial bed step, leading to a rate of erosion and deposition only well captured in time and space if using Smart CFBS formula. In test case F, where both sides are initially filled with water, and a favorable slope is present, only Smart CFBS formula leads to a correct erosion evolution in time, that becomes negligible in the final stage of the experiment. From this set of test cases it can be concluded that Smart CFBS formula can be recommended for dam break test cases with null, adverse and favorable slopes, and wet/dry problems.

When numerically modeling dam erosion and failure it has been found that Smart CFBS formula is applicable in all cases analyzed in this study. Also, Engelund and Fredsoe capacity formula provides correct results in bed level predictions, although Smart CFBS formula estimates much better the maximum discharge values reached in all experiments. It is also worth mentioning that, for downstream steep slopes, the computational time associated to the peak discharge value is calculated earlier.

The computed sand cube test showed that the best agreement between experimental and numerical data are obtained with Smart (computing slope as friction slope) and Smart CFBS. This can be explained considering that, in this case, unsteady hydrodynamic effects are a quasi-steady process of slowly varying bed-load, and friction slope is adapted to bed slope.

2D test cases

For the first experiment, the dike failure by overtopping, characterized by a one-dimensional flow, it was clearly stated that the Smart CFBS formulation provides the most accurate results in time and in space.

In the second experiment, a symmetric dam break over a mobile bed in a channel with an enlargement zone was numerically reproduced. In this case a two-dimensional flow is generated and differences among different sediment formulations are less noticeable. Numerical results follow the tendency of the final bed morphology, underestimating the length of the diamond-shaped body and the thickness of the eroded layer. In the third experiment, where an erodible channel with a sudden enlargement produces a two-dimensional flow, the computational results provided good agreement with experimental values for the different sediment formulae.

Comparing with previous results from other authors (Spinewine & Zech, 2004; Abderrezzak & Paquier, 2011; Wu & Wang, 2007, 2008) it can be stated that the numerical scheme used in this work allows to clarify the differences among different formulations which were derived by 1D stationary laboratory experiments.

The Smart CFBS discretization reaches the more accurate results in all cases, although in a genuinely 2D flow, that is, a situation involving more than one flow direction, the differences between sediment transport formulae are not as noticeable as in the 1D situations.

7.2 Further research

Numerical experimentation is necessary to include non-equilibrium state formulation in the mathematical model. Hence, it is necessary to develop the one layer model derived of mass conservation equations, section 2.3.1, which included a non uniform density along the longitudinal profile. Several authors have suggested to include the difference between the actual transported material and the equilibrium sediment transport capacity by means of the definition of an adaptation length.

The inclusion of the suspended transport coupled with the bed load model developed here is other natural follow-up of this work. For this phenomenon, both mathematical and numerical model are still to be studied.

The study of the mathematical and numerical properties of more complex friction laws for the definition of the shear stress at the bottom is also necessary. This feature is oriented to the definition of a hyperconcentrated model, where the rheology of the flow presents a pseudo plastic behavior due to high values of depth averaged concentrations.

Applications to flood events, where the bed topology is dramatically modified by the flow are still to be studied.

Bibliography

Abderrezzak, K. K. & Paquier, A. 2011 Applicability of sediment transport capacity formulas to dam-break flows over movable beds. *Journal of Hydraulic Engineering* **137**, 209–221.

Armanini, A. & Di Silvio, G. 1988 A one-dimensional model for the transport of a sediment mixture in non-equilibrium conditions. *Journal of Hydraulic Res.* **26**, 275–292.

Ashida, K. & Michiue, M. 1972 Study on hydraulic resistance and bedload transport rate in alluvial streams. *Transactions, Japan Soc. Civil Eng.* **206**, 569–589.

Begnudelli, L., Valiani, A. & Sanders, B. F. 2010 A balanced treatment of secondary currents, turbulence and dispersion in a depth-integrated hydrodynamic and bed deformation model for channel bends. *Advances in Water Resources* **33**, 17–33.

Camenen, B. & Larson, M. 2005 A general formula for non-cohesive bed load sediment transport. *Estuarine, Coastal and Shelf Science* **63**, 249–260.

Cunge, J.A., Holly, F.M. & Vervey, A. 1980 *Practical Aspects of Computational River Hydraulics*. Pitman: London.

De Vriend, H.J., Zyserman, J., Nicholson, J., Roelvink, J.A., Pechon, P. & Southgate, H.N. 1993 Medium-term 2dh coastal area modelling. *J. Coast. Eng.* **21**, 193–224.

Dressler, R. F. 1954 Comparison of theories and experiments for the hydraulic dam-break wave. *Int. Assoc. Sci. Hydrology* **3**, 319–328.

Einstein, H.A. 1950 *The bed-load function for sediment transportation in open channel flows*. Tech. Rep.

Engelund, F. & Fredsoe, J. 1976 Sediment transport model for straight alluvial channels. *Nordic Hydrology* **7,Issue 5**, 293–306.

Fraccarollo, L. & Capart, H. 2002 Riemann wave description of erosional dam-break flows. *Journal of Fluid Mechanics* **461**, 115–133.

Grass, A. 1981 *Sediments transport by waves and currents*. SERC London Cent. Mar. Technol, Report No. FL.

Greimann, B., Lai, Y. & J., Huang 2008 Two-dimensional total sediment load model equations. *J. of Hydraulic Res., ASCE.* **134**, 1142–1146.

Hudson, J. 2001 *Numerical techniques for morphodynamic modelling*. Ph.D. thesis, Department of Mathematics, The University of Reading, Whiteknigths, Reading.

Kalinske, A. 1947 Movement of sediment as bed load in rivers. *J. of Trasns. Hydr. Engineering* **28**, 615–620.

Luque, R. Fernandez & van Beek, R. 1976 Erosion and transport of bedload sediment. *J. Hydraulics Res.* **14**, 127–144.

Meyer-Peter, E. & Müller, R. 1948 *In: Report on the 2nd Meeting International Association Hydraulic Structure Research*. Stockholm, Sweden.

Murillo, J. & García-Navarro, P. 2010 An exner-based coupled model for two-dimensional transient flow over erodible bed. *Journal of Computational Physics* **229**, 8704–8732.

Murillo, J., García-Navarro, P. & Burguete, J. 2009 Conservative numerical simulation of multicomponent transport in two-dimensional unsteady shallow water flow. *Journal of Computational Physics* **228**, 5539–5573.

Nielsen, P. 1992 *Coastal Bottom Boundary Layers and Sediment Transport. Advanced Series on Ocean Engineering*. World Scientific Publishing.

Parker, G. 1979 Hydraulic geometry of active gravel rivers. *Journal of Hydraulic Engineering* **105**, Issue 9.

Peña, E., Fe, J., Sánchez-Tembleque, F., Puertas, J. & Cea, L. 2008 Experimental validation of a sediment transport two-dimensional depth-averaged numerical model using piv and 3d scanning technologies. *Journal of Hydraulic Research* **Vol. 46**, 489–503.

Roe, P.L. 1986 *Numerical Methods in Fluid Dynamics*. Vol II. Oxford University Press, Oxford.

Rosatti, G., Murillo, J. & Fraccarollo, L. 2007 Generalized roe schemes for 1d two-phase, free-surface flows over a mobile bed. *Journal of Computational Physics* **54**, 543–590.

Smart, G. 1984 Sediment transport formula for steep channels. *Journal of Hydraulic Engineering* **3**, 267–276.

Soares, S., Poncin, M., Paquier, V., Spinewine, B. & Zech, Y. – *Pire workshop dam-break flow on mobile bed* **-**, –.

Spinewine, B. & Zech, Y. 2004 *Proc., 4th Workshop of IMPACT Project*. alkema, Rotterdam, The Netherlands.

Spinewine, B. & Zech, Y. 2007 Small-scale laboratory dam-break waves on movable beds. *Journal of Hydraulic Research* **45**, 73–86.

Tingsanchali, T. & Chinnarasri, C. 2001 Numerical modelling of dam failure due to flow overtopping. *Hydrological Sciences-Journal-des Sciences Hydrologiques* **46**, 113–130.

Toro, E.F. 2001 *Shock-Capturing Methods for Free-Surface Shallow Flows*. Wiley, New York.

Wong, M. 2003 Does the bedload transport relation of meyer-peter and müller fits its own data? *Proc., 30th IAHR-Congress, Thessaloniki, Greece* p. 8 pp.

Wu, W. 2007 *Computational river dynamics*. Taylor and Francis.

Wu, W. & Wang, S.S.Y. 2004 Depth averaged two dimensional numerical modelling of unsteady flow and non uniform sediment transport in open channels. *Journal of Hydraulic Engineering* **130**, 1013–1024.

Wu, W. & Wang, S.S.Y. 2007 One-dimensional modeling of dam-break flow over movable beds. *Journal of Hydraulic Engineering* **133**, 48–58.

Wu, W. & Wang, S.S.Y. 2008 One-dimensional explicit finite-volume model for sediment transport with transient flows over movable beds. *Journal of Hydraulic research* **46**, 87–98.

Xia, J., Lin, B. Falconer & R.A., Wang, G 2010 Modelling dam-break flows over mobile beds using a 2d coupled approach. *Advances in Water Resources* **33**, 171–183.

Z. Cao, R. Day, S. Egashira 2002 Coupled and decoupled numerical modeling of flow and morphological evolution in alluvial rivers. *Journal of Hydraulic engineering* **128**, 306–321.